MASTER THESIS

GridPix

Data Analysis of Measurements on a GridPix detector

Lucie de Nooij

UNIVERSITEIT VAN AMSTERDAM

NIKHEF

Master Physics: Particle and Astroparticle Physics
NIKHEF, National Institute for Subatomic Physics
University of Amsterdam
January 2009

Supervisor:
dr. J. Timmermans
National Institute for Subatomic Physics
Detector R & D department
e-mail: i06@nikhef.nl

Supervisor:
dr. A.P. Colijn
National Institute for Subatomic Physics
ATLAS department
e-mail: z37@nikhef.nl

Aan een aanstaande fysica,

Zoek vooruitgang om het draaien van de aarde

zoek het begin in sterren die opgaan in zichzelf, deel

tot de ondeelbaarheid, tot klein niet kleiner kan

tot het tegendeel van het bestaan, elke boom stoel wordt

elke koe biefstuk of leren bank.

Geef ons onmisbaarheid die we nog niet kennen

geef ons onzichtbaarheid die vliegt langs ondergrondse kilometers

geef ons leven met de snelste ontvangst

geef ons fietslampjes, laat ons zien met ogen van laser.

Froukje van der Ploeg

Voor Oma Lucie

Abstract

The GridPix detector, a micro pattern gaseous detector developed at Nikhef, consists of a gaseous volume and an amplification grid on a CMOS TimePix chip. This new detector can be a main option for high-precision tracking at the International Linear Collider. Cosmic muon data are taken with a GridPix placed in a magnet field at Nikhef, Amsterdam. A beam test is conducted at PS/T9, CERN, Geneva. The transverse diffusion decreases significantly when using argon 3% CF_4 2% isobutane under the influence of a magnetic field, although less than expected from MAGBOLTZ calculations. The error on the measured zero point resolution is large due to a delay between the passage of the charged particle and trigger and time slewing effects. Energy loss measurements allow a distinction between electrons and pions up to a confidence level of 4.4 σ with 25 cm of combined track lengths in helium 20% isobutane.

Contents

Introduction

Particle physics studies the building blocks of matter and the forces between these building blocks. Apart from the elementary particles that build up all ordinary matter around us, Nature provides more. More exotic particles can be produced in the universe and can penetrate the Earth's atmosphere where they are studied by astro-particle physicists. To study the heavier exotics in more detail, scientists have built several particle accelerators over the last decades. At the moment of writing, the Large Hadron Collider (LHC) in Geneva, Switzerland, is almost ready for data taking. In the LHC proton-proton collisions will take place, producing a range of interesting, and uninteresting, processes. The search for new processes in this jungle of collision products will be challenging and very exciting.

The particles produced in the LHC and the cosmos should not go unnoticed, but can not be seen by eye. Therefore physicists have come up with different ways to detect these particles (in)directly. Like the eye is a detector for light of specific wavelengths, detectors are used to measure position and energy of particles. Such detectors consist of some medium (solid state, gas or a liquid), where the particles produce a signal during passage, and signal readout. This readout was originally done by eye, ear, or with a counter. When count rates raised and measuring times lasted longer, this human read out became less practical. Nowadays, most detectors are read out electronically. Measurements became faster, with better resolution and data easier to handle and store.

This thesis is the report of my master project for the master of particle and astro-particle physics at University of Amsterdam. The research was conducted with a new type of gaseous detector with a digital chip for readout. This detector measures the tracks of charged particles with potentially a very good resolution and sensitivity. This detector, named GridPix, can find a wide range of applications and is a possible candidate for a sub-detector at the future International Linear Collider (ILC). In chapter 1 the reader can find more information on the ILC. Chapter 2 provides an introduction to the time projection chamber (TPC) and GridPix, as well as background information on energy loss by particles in matter and drift of electrons under the influence of an electric field. The different analysis and reconstruction steps done in this research are explained in chapter 3. In chapter 4 the results of the analysis are presented and discussed. Chapter 5 sums the conclusions that can be drawn from this work and chapter 6 provides an outlook.

Chapter 1

International Linear Collider

This chapter provides some information needed on the International Linear Collider (ILC) for understanding a possible wider context of this thesis. We will first discuss the physics expectations in the newly reached energy levels at the LHC and its influence on and by the ILC. Then provide some detail on the machine's parameters and go into modest detail on the detector designs and the possible purpose of GridPix detectors in that. In section 1.4 some elements of the ILC software framework are discussed.

1.1 New Physics at new energies

More detail is seen in the structure of matter using higher energy probes. In the next few years, the experiments at CERN's LHC will have a direct look at the Terascale physics. Possible discoveries include the Higgs boson, evidence for extra dimensions or the observation of supersymmetric particles.

The proton-proton collisions in the LHC will provide particle physicists with a huge amount of information [1]. A wide range of constituent collision energies up to 2 TeV will be thoroughly scanned. One of the searches at the LHC will be for the (Standard Model) Higgs. But while finding the Higgs in the vast amount of data from the LHC will be a highly demanding job, examining its detailed properties will be sheer impossible. That is why scientists are anticipating on the construction of the ILC, International Linear Collider, in which electrons will collide with their anti-particles, positrons. These collisions will be much cleaner, and with the LHC suggesting in what energy range to look, the characteristics of the new particles can be investigated. If there is more than one decay channel of the Higgs, the LHC experiments will determine the ratio of the branching fractions; the ILC can measure these couplings to a few percent, revealing whether the Higgs is a Standard Model particle or something more complex.

With combined effort, the LHC and ILC may reveal the existence and characteristics of extra dimensions, super-symmetric particles and Dark Matter candidates [2].

1.2 The machine: some numbers

In order to reach the centre-of-mass energy of $\sqrt{s} = 500$ GeV aimed for, the ILC will be approximately 31 kilometres long, plus two damping rings of 6.7 kilometres circumference each. See figure 1.1 for an artist impression of the future accelerator complex. These damping rings are

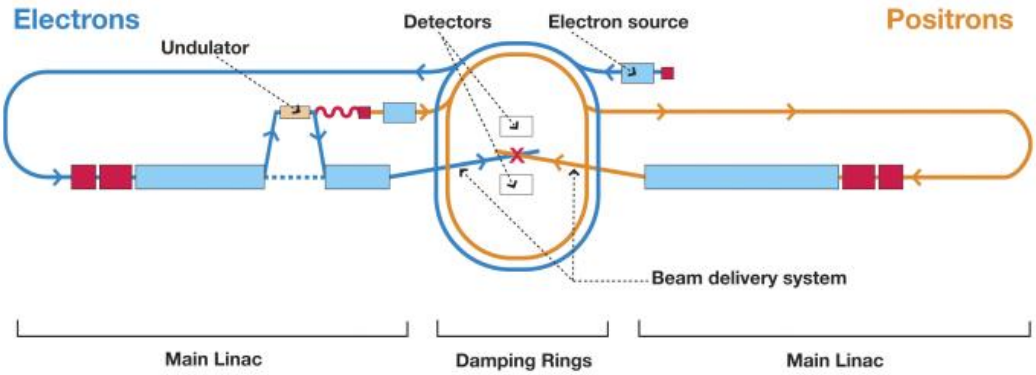

Figure 1.1: An artist impression of the ILC accelerator complex, with its damping rings and total length of 31 kilometre. An undulator is used to force electrons to oscillate and radiate for the production of positrons. This picture is not to scale. More information on this picture can be found in[4].

used to focus the bunches in about 10.000 rounds into bunches with the diameter of a human hair [3]. The centre-of-mass energy of 500 GeV needs an average accelerating gradient in the superconducting radiofrequency cavities of 31.5 MV/m.

In November 2004, the first ILC Workshop was held at KEK, Tsukuba, Japan. At the second Workshop in August 2005, the ILC Global Design Effort (GDE) was officially formed. The most costly parts of the accelerator itself comprises the design and construction of the cavities and the cost of conventional facilities, such as civil engineering. The primary challenge for the ILC R&D will be the achievement of the 31.5 MV/m as the operational accelerating gradient. The GDE's goal is to present an engineering design study by 2012, allowing for the high energy physics community to seek project approvals and get started with the construction by 2014. This would permit operations to begin in 2021 [2].

1.3 The detectors

The ILC experiments will not only search to understand the predicted mass generation mechanisms and super-symmetric particles, but also for the unpredicted. In order to detect an invisible particle, e.g. a Dark Matter candidate, the detectors need to measure missing energy up to a high precision, up to a factor of 2 better than at LEP or SLC[5]. At present three different detector designs are suggested[6], which differ in approach and technology choices, but have their overall structure in common. The first concept, the Silicon Detector (SiD), has a full silicon tracking system and Particle Flow oriented calorimetry. The second, the International Linear Collider Detector (ILD) has a TPC as main tracker and is a merge between two initial concepts. The third, the 4^{th} concept, has a tracking system in which both silicon and gas are used, a "double readout" calorimeter system and includes a double solenoid magnet system. Each concept consists of an inner vertex detector, a tracking system based on a gaseous TPC or silicon detectors, a calorimeter, a muon system and a forward tracking system. The main differences between detectors consider the strength and extent of the magnetic field, the inner and outer radii of the sub-detectors and the calorimeter technology. See also table 1.1. The calorimeters will be surrounding the vertex and tracking detectors, so the particles from the collisions should lose as little energy as possible before being stopped in the calorimeters. No

	ILD	SiD	4^{th}
Vertex	pixel	pixel	pixel
inner radius (cm)	1.8	1.5	1.5
outer radius (cm)	6.0	6.1	6.1
Main tracker	TPC/Si	Si	TPC/drift
inner radius (cm)	40	20	20
outer radius (cm)	160	127	140
Magnet			
type	main	main	inner/outer
field strength (T)	3	5	3.5/-1.5
radius (cm)	350	250	300/550
Overall detector			
radius (cm)	660	645	550
half-length	690	589	650

Table 1.1: A few parameters of the ILC detector concepts.

matter which design is chosen, the best spatial and energy resolution possible will be needed to achieve the research goals set for the ILC. With the digital TPC used for this thesis a much better spatial and energy loss resolution can possibly be achieved and with gas as an active medium it is light. This makes these devices a main option for high-precision tracking at the ILC [7].

1.4 The ILC software framework

At present all groups in the ILC TPC community use their own analysis software. This is time consuming due to possible double work and makes the comparison of results error prone. A combined effort is made to develop a software framework shared among the ILC TPC community to ensure the quality of the algorithms and allow faster and easier comparison of results [8].

To standardise the exchange of data, the LCIO (linear collider input/output) persistency framework [9] was developed. It offers a way to store and use data in a fast and independent way. To share simulation, reconstruction and analysis code, the Marlin framework can be used [10]. Within the Marlin framework each individual step of the reconstruction is done with a so-called processor. These processors all make use of the same sets of parameters, obtained from GEAR [11] and LCCD [12], for geometry and calibration data respectively.

Chapter 2

Micro Pattern Gaseous Detectors

In this chapter the time projection chamber and the micro pattern gaseous detector are introduced. Next the physical processes enabling tracking charged particles in a gaseous detector are discussed. Charged particles can be detected in a gas, because they ionise the gas molecules along their trajectory. The electrons liberated in doing so, are drifted through the gas and amplified for read out. In this chapter we will discuss how much ionisation is created by a charged particle theoretically and the energy loss associated with the ionisations. We will discuss the electrons' drift towards the anode and the diffusion, resulting in a non-straight drift path. We will also touch upon the influence of the electric and magnetic field in the drift volume on the drift and diffusion. The next chapters may use this chapter as a reference, therefore only information applicable to this research is discussed. For a more comprehensive discussion of all the above mentioned, the reader is referred to e.g. [13] or [14].

2.1 Time Projection Chamber

In 1978 Dave Nygren of the Lawrence Berkeley Laboratory invented a new detector to measure the trajectories of charged particles [15]. This detector, named time projection chamber (TPC), has proven itself to be very useful in particle physics experiments ever since because of it's 3D track localisation, enabling tracking in high-track-density environments, and for identifying particles through their energy loss. The TPC's first major application was in the PEP-4 detector, at the PEP storage ring at SLAC[16].

In general a TPC is a drift chamber, a gaseous volume, in which charged particles leave a trail of ionised molecules and electrons along their flight trajectory. When an electric field is applied, the electrons will drift towards the anode and the ions towards the cathode. At the anode electrons are read out, mostly after amplification. The PEP-4 TPC's cathode was a central membrane so the ionisation electrons drifted to one of the two end caps. A magnetic field was used to minimise transverse diffusion and bend the trajectories of the traversing particles for momentum measurement, see also section 2.5. The end caps were divided into six sectors, each containing a 183-anode multiwire proportional chamber (MWPC). The drifted electrons were accelerated in the strong field around the wires, acquiring enough energy to ionise the gas and produce an avalanche. The signal was read out at the end of the wire.

Since 1979 the principles of the TPC have been developed for different applications. In 1988 A. Oed invented a new way to detect the drifted electrons, reducing cell size limits dramatically,

using modern photolithographic technology [17]. This new detector, a micro-pattern gaseous detector (MPGD) consisted of a set of tiny metal strips, laid on a thin insulating glass substrate. The detector proved to be very easily damaged by discharges in the gas. The more powerful gas electron multiplier, GEM [18] and MicroMEGAS [19] detectors can offer an answer to the needs of high-resolution measurements in a harsh radiation environment [7].
The MPGD used for this thesis is discussed in the next section.

2.2 GridPix

The GridPix detector is a Dutch-built MPGD from Nikhef in Amsterdam. This TPC with typically one to ten cm drift space consists of a thin chemically perforated metal grid, a MicroMEGAS, above an active anode, the readout chip, which is mounted on a printed circuit board (PCB). See figure 2.1 for a picture of one of the detectors used in this thesis which broke down during operation. This detector differs from other MicroMEGAS MPGDs because the grid is mounted on the chip in a photolithographic post processing step. After this process, the holes of the grid are located exactly above the readout pixels, avoiding unwanted interference patterns between the holes in the grid and the pixels. For reliable operation of this detector a homogeneous electric field and discharge protection of the chip is needed. Both issues are discussed here.

In order to keep the electric drift field as homogeneous as possible two provisions are taken. Firstly, strips are placed around the drift region. A voltage is applied to these strips, inducing the desired electric field strength for that particular distance from the cathode to the drift volume. Secondly, a guard ring is glued on the PCB. This guard ring consists of a perspex layer of about 1 mm with a kapton-copper foil on one side. By applying the desired voltage this copper foil on a distance of roughly 1 mm above the grid, the electric field lines will point straight from the cathode to the guard and grid. Without the guard, the PCB has a locally lower field so the field lines may bend outwards, causing the edges of the chip to appear blind.

In order to protect the chip from discharges a high-resistive layer of 5 μm up to 25 μm of amorphe silicon is deposited on the chip. When a discharge propagates in the gas, a charge builds up at the surface of the silicon, thus locally reducing the electric field. This quenches the discharge, spreading the charge deposited in terms of time and location. This means the total charge of the discharge is collected by more pixels and in a somewhat longer period of time. When the first chips at Nikhef post processed with amorphe silicon survived discharges in 2007, it became reasonable to start thinking about possible applications for the device.

Once the electrons have drifted through the gas, they are amplified between the grid and the chip in an electric field of about 75 kV/cm. The avalanches caused by the amplification consist of typically 1000 to 3000 electrons and are detected by the pixels on the silicon pixel device TimePix.

The TimePix chip was developed at CERN as a modification of the Medipix chip. The chip is equipped with 256 x 256 square pixels of 55 x 55 $(\mu m)^2$, each connected to its respective pre-amplifier, discriminator and digital counter. Each pixel can work in one of three modes:

Medipix mode - Each pixel counts the number of incoming electrons during a predefined time interval.

Time mode - Each pixel counts the number of 10 ns clock cycles from the signal crossing of

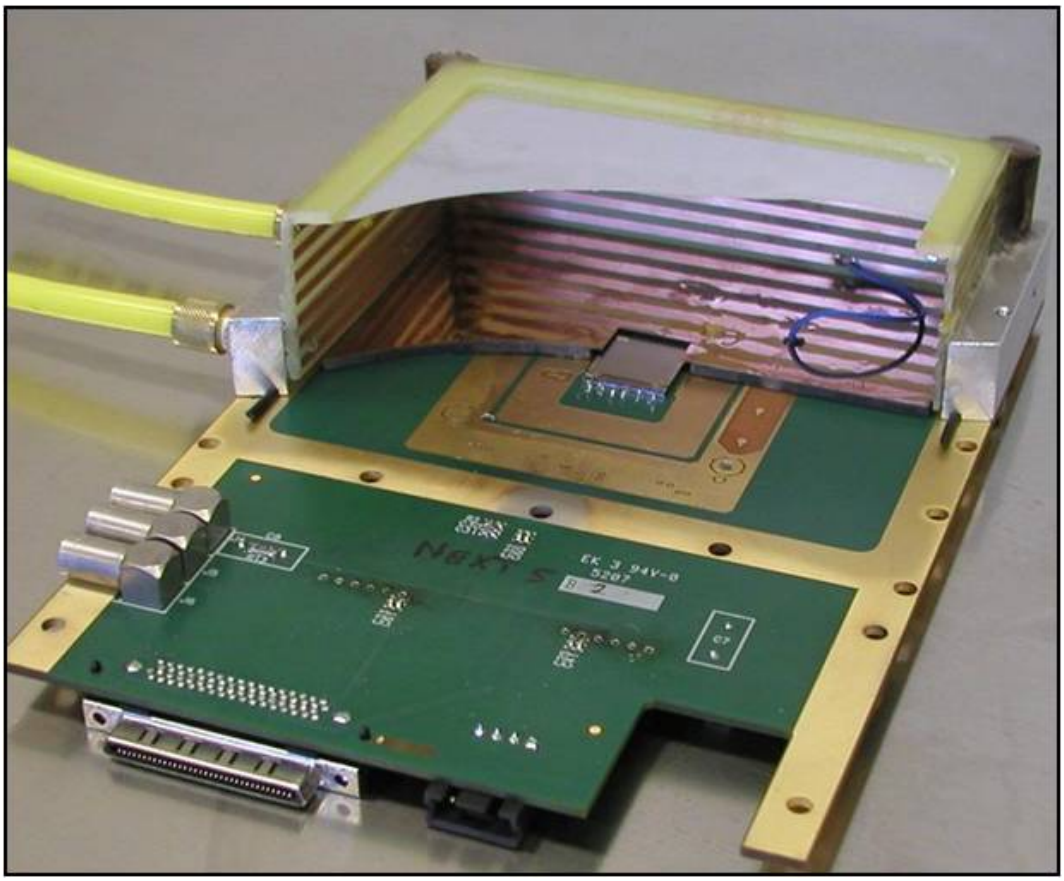

Figure 2.1: A photo of one of the GridPix detectors. From top to bottom we see the cathode and the strips and guard used to create a homogeneous electric drift field. In the middle of the guard, we see the TimePix chip. The chip has dimensions of 14x16 mm, the guard of 9x11 cm and the maximum drift length is 30 mm.

the threshold to a global stop signal.

Time over threshold(TOT) mode - Each pixel is used as an ADC, providing a proportional measure for the amount of charge deposited on each pixel.

The TimePix chip is readout using a Muros2 board, an interface between a board carrying a maximum of eight TimePix chips and a National Instruments DIO-653X board. The Muros2 has been developed at NIKHEF [20]. The Muros, and thus the TimePix chip, are readout using the Pixelman software package developed at the Czech Technical University of Prague [21].

2.3 Multi pixel hits and time slewing

A single particle often creates signal in a cluster of adjacent pixels on the TimePix chip, because the charge created by the avalanche is spreading out during the charge collection process [22]. This effect is possibly reinforced by the amorphe silicon layer. In this thesis such clusters are referred to as *multi pixel hits*. It is reasonable to assume that the charge collected in the adjacent pixels is smaller than in the pixel that originally fired. If the threshold for both pixels is the same and the charge is collected in the same time span, the signal from the pixel with the

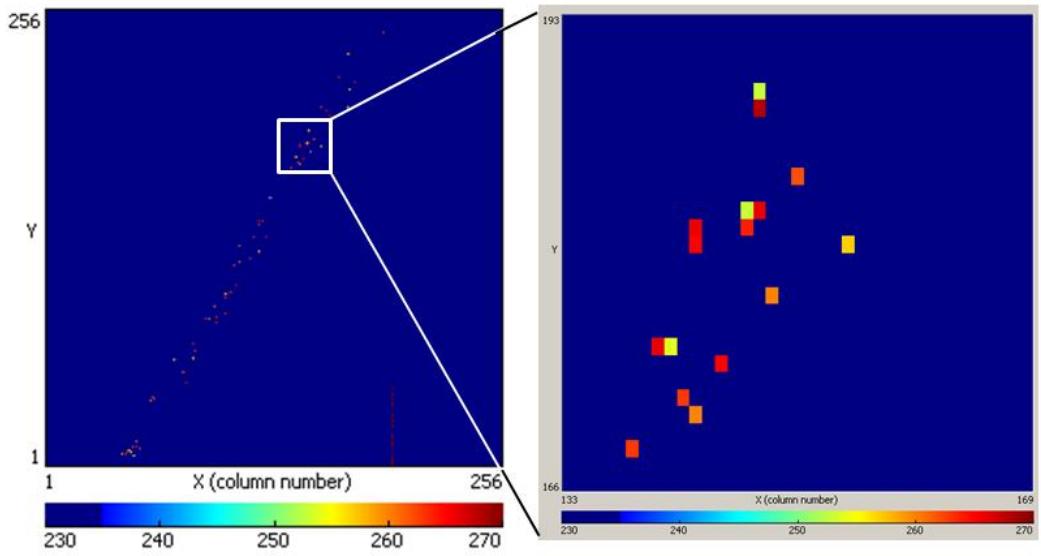

Figure 2.2: In this figure a Pixelman output of a track from run 02030103 is shown on the left. On the right is zoomed in on the square. A few multi pixel hits are clearly visible. The time difference is seen a the colours of the hits are different. The redder the colour, the larger the value content of the pixel and the closer to the chip the hit was produced. The time difference in counts between the multi pixel hit in the centre of the right image is 13 counts.

smallest amount of charge will appear to have arrived later. See figure 2.2 for an example of a track with multi pixel hits. This is due to the smaller slopes of the smaller signal. This delaying process is referred to as *time slewing*. See figure 2.3 for a quantitative measure of the time slewing from[23]. Because of time slewing, multi pixel hits can be tracked in the data and possibly removed before analysis. The reader is referred to section 3.3 for this selection of data.

2.4 Creating Tracks: Energy loss

A charged particle traversing the gas of a drift chamber will leave a track of ionisations along its flight trajectory. The occurrence of an ionisation is random and depends on the mean free path between collisions in the specific gas. The mean free path λ_e can be deduced from the ionising cross-section per electron σ_i and N_i, the number of gas molecules per volume:

$$\lambda_e = \frac{1}{N_i \sigma_i}. \tag{2.1}$$

The value of λ_e depends on the pressure and mixture of the gas and the particle's velocity. The value of λ_e for a gas mixture can be calculated from the values of N_i and σ_i of the pure gases in the mixture. When the charged particle encounters a gaseous molecule, it can transfer energy to the molecule in roughly four different ways:

- One or more electrons are ejected from the molecule, the liberated electrons do not have enough energy to cause other ionisations themselves.
- One or more electrons are ejected from the molecule, the liberated electrons have enough energy to ionise other molecules. Consequently, the primary electrons liberate other electrons and a cluster of electrons is formed.

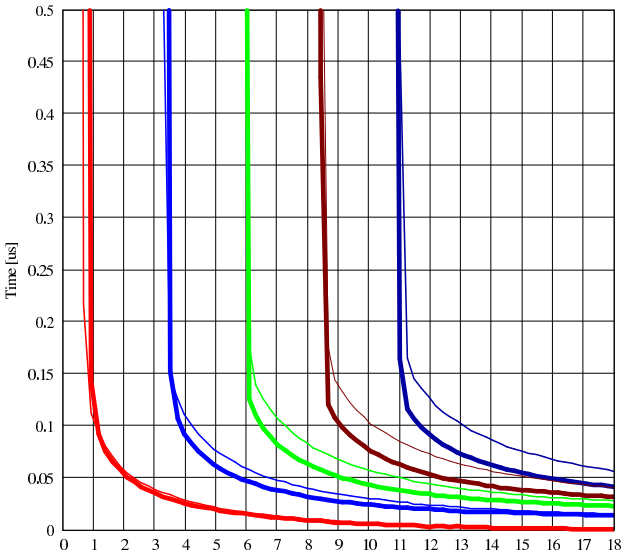

Figure 2.3: Time slewing of one pixel in the centre of a TimePix chip. On the horizontal axis we see the incoming charge expressed in thousands electrons. In our case, the total number of electrons is some 2500 per avalanche, which means that the expected time slewing in that case is about 0.04 μsec, which is 40ns or 4 counts. The variance on the number of incoming electrons introduces an uncertainty on the time slewing and thus the time measurement.

- The liberated electron has enough energy to create its own track, a *δ-ray*.
- Apart from a possible electron being liberated, the molecule is left in an excited state. When the molecule falls back into its ground state, it may radiate a photon. The photon may cause an ionisation or can be caught by a molecule of an organic gas, in this context called *quencher*.

The primary electrons are emitted almost perpendicular to the track. Before they lose their kinetic energy, they may travel a distance of about 30 μm (if their energy is 1 keV) to 1.5 mm (10 keV). More than 90% of the liberated electrons have an energy in the 1 to 3 keV energy range.

Only a fraction of the energy lost by the traversing particle is used for ionisation. The total amount of ionisation depends on W_i, the average energy lost when creating one electron:

$$W_i\langle N_i\rangle = L\langle\frac{dE}{dx}\rangle, \tag{2.2}$$

with $\langle N_i\rangle$ the average number of electrons created along a trajectory of length L and $\langle\frac{dE}{dx}\rangle$ the average total energy loss per unit path length. W_i must be measured for every gas mixture.

To calculate the $\langle\frac{dE}{dx}\rangle$ the Bethe-Bloch equation is generally used:

$$-\frac{dE}{dx} = \left(\frac{4\pi r_e^2 m_e c^2 N_0 Z z^2}{A\beta^2}\right)\left\{ln\left[\frac{2m_e c^2\beta^2}{(1-\beta^2)I}\right] - \beta^2\right\}, \tag{2.3}$$

where N_0 is Avogadro's number, Z and A the atomic and mass number of the gas mixture, I the ionisation potential, m_e the electron mass and r_e the classical electron radius, z the charge

and βc the velocity of the fast particle. Units are in MeV $g^{-1}cm^2$.

The energy lost by the fast particle at every collision with a gaseous molecule is very small with respect to its total energy. Therefore, the number of ionising collisions is described by Poisson statistics and the distance l between successive collisions can be described as:

$$p(l) = 1/\lambda_p \cdot e^{-l/\lambda_p}, \tag{2.4}$$

where λ_p is the ionisation mean free path. The number of collisions per unit length depends on the type and momentum of the fast particle, temperature, pressure and gas mixture.

2.5 Drift and diffusion

Once liberated, either by the fast particle or by another electron, the electrons will drift towards the anode under the influence of an electric field. During the movement through the gas, the electrons will randomly collide with the gaseous molecules. Due to these collisions the projected position of the electron may differ from the point of creation. The diffusion constant D in units of cm^2/s is defined by the Gaussian density distribution of the probability of the collisions. This makes the mean squared deviation of the electrons equal to $2Dt$ in any direction from the centre, with t the drifted time. The standard deviation of this distribution in one coordinate is $\sigma = \sqrt{2Dt}$. Or $\sigma = \sqrt{2Dz}$, with $z = v_D t$ the drifted distance, with v_D the drift velocity of the electrons. When projected on a plane, the factor of $\sqrt{2}$ cancels out. The standard deviations along the transverse and longitudinal components of the drift are therefore:

$$\sigma_t = D_t\sqrt{z} \quad \text{and} \quad \sigma_\ell = D_\ell\sqrt{z}, \tag{2.5}$$

with D_t and D_ℓ usually expressed in $\mu m/\sqrt{cm}$.

The drift velocity and D_t and D_ℓ are dependent on the density and mixture of the gas and the strength of the electric drift field. This is a non-linear dependence and for every value of the electric field, the value for D_t must be calculated separately. When in this thesis is referred to "expected values" in this context, I mean to refer to generated parameters by the program MAGBOLTZ [24].

It is very possible that in the drift volume the drift and diffusion of the electrons are not only influenced by an electric field, but also by a magnetic field. The magnetic field may be used to bend the trajectory of the fast particles, allowing a reconstruction of their momenta. When the magnetic field is in the direction of the electric drift field, it can lower the D_t. How much it may decrease depends on the density and mixture of the gas.

In the presence of both an electric and magnetic field the electrons will be subject to a Lorentz force in the direction perpendicular to their drift velocity:

$$\vec{F_L} = q(\vec{E} + \vec{v_D} \times \vec{B}). \tag{2.6}$$

When the magnetic and electric field are in the same direction, the electrons will spiral along the magnetic field lines with a cyclotron frequency ω of:

$$\omega = -\frac{qB}{m}, \tag{2.7}$$

with q the charge of the electron, B the strength of the magnetic field and m the mass of the electron. This will effectively diminish the transverse diffusion. So when the magnetic field is applied, the expected diffusion constants read:

$$D_{t,\vec{B}} = \frac{D_t}{(1+\tau_e^2\omega^2)} \quad \text{and} \quad D_{\ell,\vec{B}} = D_\ell[13], \tag{2.8}$$

with τ_e:

$$\tau_e = \frac{\lambda_e}{v_D}, \tag{2.9}$$

the mean free time between collisions.

With no magnetic field applied, the drift velocity points in the direction of the electric field:

$$\vec{v_D} = \frac{q}{m}\tau_e\vec{E}. \tag{2.10}$$

In the presence of a magnetic field, the magnitude of $\vec{v_D}$ is reduced by a factor:

$$\frac{v_D(\omega)}{v_D(0)} = \left(\frac{1+\tau_e^2\omega^2 cos\phi}{1+\tau_e^2\omega^2}\right)^{1/2}, \tag{2.11}$$

where ϕ is the angle between $\vec{E}$ and $\vec{B}$. Equation 2.11 predicts that the drift velocity is unaffected by the presence of a magnetic field if it is oriented parallel to the electric field. This was the case for all measurements done for this thesis.

2.6 Silicon versus Gas

As mentioned in section 1.3, the MPGDs used for this research can be a main option for high-precision tracking at the ILC. Nowadays, semiconductor detectors are mainly used for tracking in high track-density environments, because 1) these detectors can be operated with a speed comparable to that of wire chambers, 2) the resolution is good and 3) their density is relatively high, allowing particles to create electron-hole pairs in small dimensions. Some disadvantages of these detectors are that 1) they are susceptible to radiation damage, 2) they consume a high amount of power, 3) they are massive and 4) require cooling. In comparison, MPGDs can potentially yield the same resolution, they are lighter, thus allowing better energy reconstruction. Besides, the pre-amp input capacity is low and no external bias current is needed. Gas can be exchanged, if it is damaged by irradiation. The research on MPGDs in terms of human and financial resources is relatively low, resulting in slower progress in R&D. Characteristics of the MPGDs that need investigation are the occurrence of sparks, the ageing of detectors and the limitation of drift length by the diffusion.

Chapter 3

Measurements and Analysis

In this chapter the reader is informed on the measurements and the different analysis steps as performed by the software. These steps include the possible removal of multi pixel hits, the track recognition using a Hough Transform and the fitting of the tracks. The software is used to measure the spatial resolution and the energy loss of the fast particles.

3.1 Operating conditions

The data used for this thesis were taken in different spaces of time between January and June 2008. From January until April 2008 cosmic muon data were taken at Nikhef in Amsterdam for analysing the influence of a magnetic field. All magnetic elements of the detector were substituted or removed and the Muros2 was placed outside the stray field of the magnet. For triggering, two scintillating detectors were connected via a photo multiplier tube to a logic gate that provided a gate opening for the Muros2 interface in case of a coincidence between the scintillators. The upper scintillator was placed such that a cosmic would only pass both scintillators when its path is 'a little diagonal' with respect to the anode. If the trajectory would be perpendicular to the chip, the projection of the path would be a dot, which is not easy to analyse. The second scintillator was placed underneath the magnet, providing a momentum cut on the coincidences, due to the iron the muons need to traverse. See figure 3.1 for a schematic example of the coincidence setup used at Nikhef. The PC reads out the chip with a frequency of 1 Hz. When a gate opening occurs during this read out, the data are written to disk. This resulted in a total of one or two gate coincidences every minute, of which 20% produced a track visible on the chip. The total time lost between the passage of the muon through the second scintillator and the

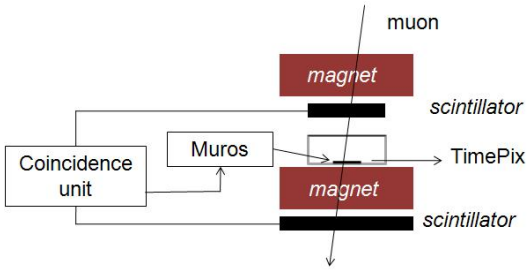

Figure 3.1: A sketch of the coincidence setup as used at Nikhef. The lower magnet foot ensured a cut on muon momentum.

gas	E_{drift} (V/cm)	-V_{grid} (V)	B Field (T)
helium 23% isobutane	600	420	0 / 0.5 / 1
argon 20% isobutane	600	380	0 / 0.5 / 1
argon 3% CF_4 2% isobutane	200	305	0 / 0.5 / 1

Table 3.1: Measurements performed at Nikhef.

gate opening is estimated to be 100 ns. During the data taking at Nikhef three different gases and magnetic field strengths were used. The electric drift and gain field strengths were kept constant for different measurements in the same gas. In this way the influence on the diffusion by the magnetic field is easily investigated. See table 3.1 for all measurements performed at Nikhef.

From 17 until 27 May 2008 a beam test was conducted at PS/T9, CERN, Geneva. See figure 3.2 for a photo of the experimental setup at Nikhef and CERN. At CERN the detector was placed in a 2 GeV and 5 GeV beam of pions and electrons. The set up was such that the passage of the beam was either parallel to or under a 25° angle with respect to the anode. The Muros2 was triggered using a coincidence between a scintillator in front of and behind the detector with an especially designed device lowering the total time between passage and gate opening to 13 ns, comparable to the timing resolution of the detector. The number of triggers recorded during the beam test was about 25 per minute, with the chip instaneous read out frequency of 15 Hz, resulting in more than 48.000 events during the week. The data were taken using different positions of the detector, different gases and grid voltages. See table 8.1 for the different measurements conducted at CERN.

3.2 Clock cycle distribution and drift velocity

The raw output of the detector is a Pixelman text file with three columns of numbers; the x and y -coordinate and content value ("z"-coordinate) of any pixel that fired during a gate opening. When operated in Time mode, the drift time of each detected electron is derived by multiplying the number of counted clock cycles with the time duration of every clock cycle:

$$\Delta t = (z_{max} - z_{hit}) \cdot \delta t, \tag{3.1}$$

where $\delta t = 10$ ns, z_{max} the maximum count of a specific run and z_{hit} the count of a measured hit. The total drift time can be derived by adding the delay between the coincidence and gate opening. In order to derive the drift velocity of the liberated electrons in the gas, a simple plot is made of the number of clock cycles of each hit in a file. When the fast particles enter the drift volume through the cathode and leave through the chip, the distribution of the clock cycles should be flat. The velocity is calculated by dividing the maximum drift distance by the total number of clock cycles. See figure 3.3. The MAGBOLTZ values for the drift velocities are listed in table 4.1.

3.3 Multi pixel hits

As mentioned in section 2.3 a single particle often creates signal in a cluster of adjacent pixels. A multi pixel hit is defined as two or more adjacent active pixels. Before the raw data are used for analysis, the multi pixels hits in the raw data are evaluated as a function of their mutual time difference in clock cycles. See figure 2.2 for an example of a track with multi pixel hits.

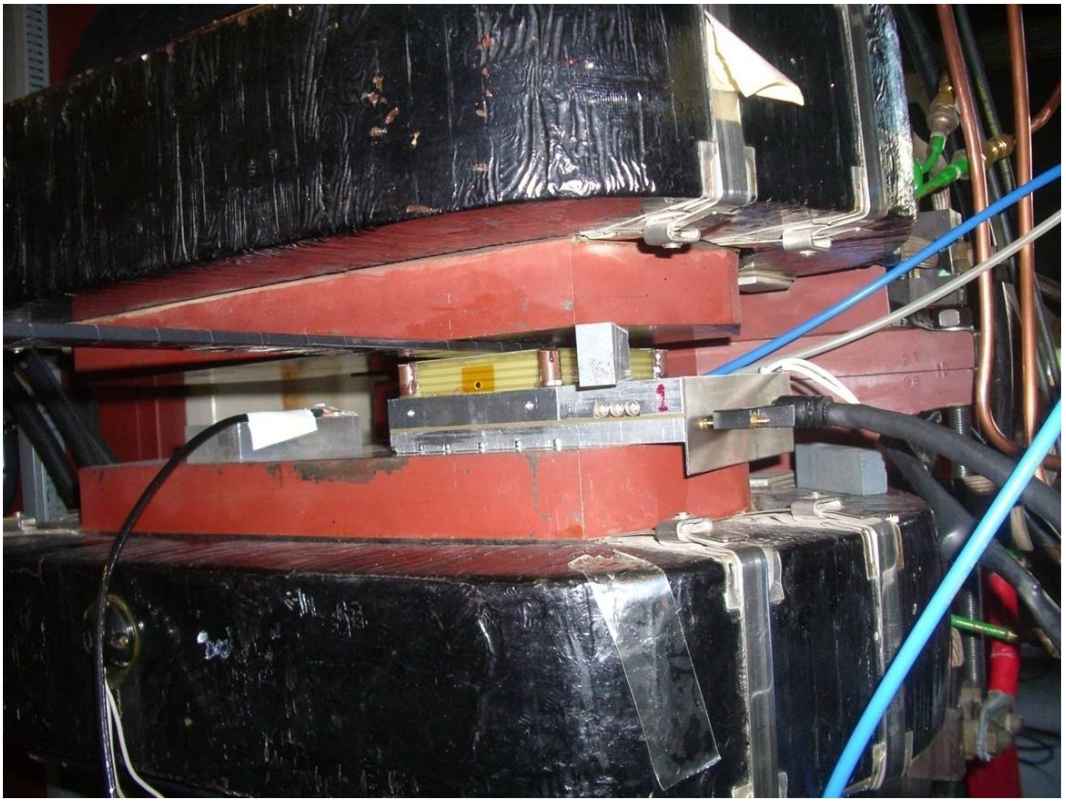

(a)

(b)

Figure 3.2: A photo of the operating conditions at Nikhef (a) and CERN (b). At Nikhef, the detector was placed inside a magnet that can produce a magnetic field of maximum 1 Tesla. In this setting the influence of a magnetic field on the transverse diffusion is tested. At CERN the detector was placed in a mixed electron/pion beam produced by the PS accelerator. In this photo the detector is placed under a 25° angle with respect to the beam.

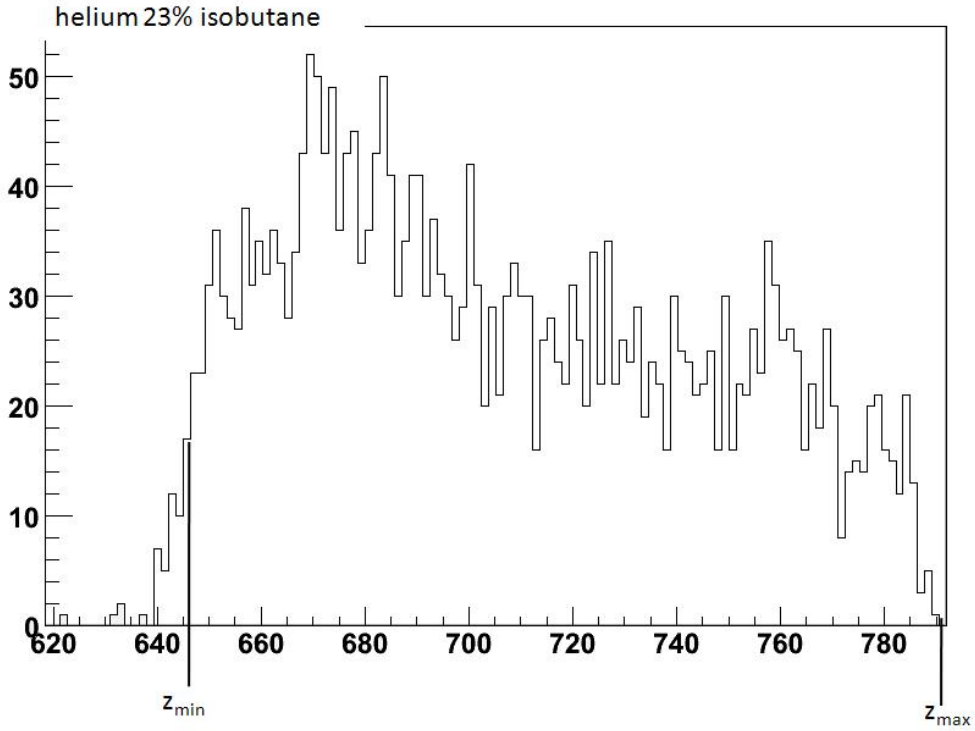

Figure 3.3: For the reconstruction of the drift velocity, the maximum drift time is measured as the difference between the maximum count, z_{max} and minimum count, z_{min}. This is counts distribution of the run helium 23% isobutane with $\vec{B} = 0$ at Nikhef. The drift velocity is found by dividing the known maximum drift length by the maximum drift time. In this case, $v_D = \frac{2.9cm}{138counts} = 2.1cm/\mu sec.$

From figure 3.4 we see that the number of multi pixel hits in the time difference range from 7 to 16 clock cycles increases from a certain grid voltage. In these cases the number of usable fits, see section 3.5, is dramatically increased if all hits that appear to have arrived later in the multi pixel hits are removed. This procedure does not seem to affect the number of usable fits in the other cases; the multi pixel hits are therefore not removed.

3.4 Track finding: Hough Transformation

In order to perform a trustable fit, it is necessary to roughly localise the tracks and their associated hits before fitting the data. When examining the beam test data, there may also be more than one track in each file, these need to be separated before fitting. For the cosmic muon data taken at Nikhef, there were no events with multiple tracks, so the pattern recognition described below was used only to exclude outliers. If outliers are included, the fitted track will be biased with respect to the fast particle's track. In this thesis a Hough Transformation (HT) algorithm is used for the recognition of the straight tracks. The input of the HT are the raw data files of Pixelman and the found tracks with their associated hits are returned for fitting.

In the (x, y) plane, a straight line can be described as $y = a + bx$, in that case the HT is a linear transformation; the straight line is parameterised in r and θ, where r is the length of the smallest possible vector from the origin to the line and θ the angle between the x-axis and this vector. Using this parameterisation, the equation of the line reads:

$$y = \left(-\frac{cos\theta}{sin\theta}\right) x + \left(\frac{r}{sin\theta}\right), \tag{3.2}$$

which can be rearranged to

$$r = xcos\theta + ysin\theta \tag{3.3}$$

For every hit in the (x, y) plane a set of 100 (r, θ) parametrisations is calculated, using equation 3.3. To do so, 100 steps are defined for $\theta \in [0, \pi]$. This means that $r \in [0, \sqrt{2}x_{max}]$. The set of (r, θ) parametrisations is described by a sinusoidal curve in the (r, θ) plane. See figure 3.5 for an example of such a parametrisation. The sinusoidal curves of points on a straight line in the (x, y) plane intercept in a single point in the (r, θ) plane. When the (r, θ) plane is divided into cells, the curves will pass through the same or adjacent cell. When the number of curves in all cells in the (r, θ) plane is counted, a maximum is found for the cell corresponding to the (r, θ) parametrisation for that straight line in the (x, y) plane. So when a two-dimensional histogram of r and θ is made, a peak is found at the cell with maximum count.

Even with only one track in the raw data, there can be more local maxima in the (r, θ) histogram. This thwarts physical meaningful peak finding in the histogram. To avoid noise, hits that are closer than 2 pixels from a particular line corresponding to a (r, θ) parameterisation can vote for that parameterisation, raising the cell of that (r, θ) pair with one. To find peaks in the (r, θ) histogram, the mean height of all bins is calculated, taking only the non-empty bins into account. Next, in an iterative process all bins lower than 70% of the mean are set empty. When less than ten bins are set to zero, the highest bin of each remaining peak is returned as possible parameterisation for a track in the (x, y) plane.

The returned (r, θ) parametrisations are examined in two ways. Firstly, the number of associated hits, hits closer than three times the expected diffusion, is counted. Secondly a cut is made on the θ of the parametrisations. In case of the beam test data, only tracks with more

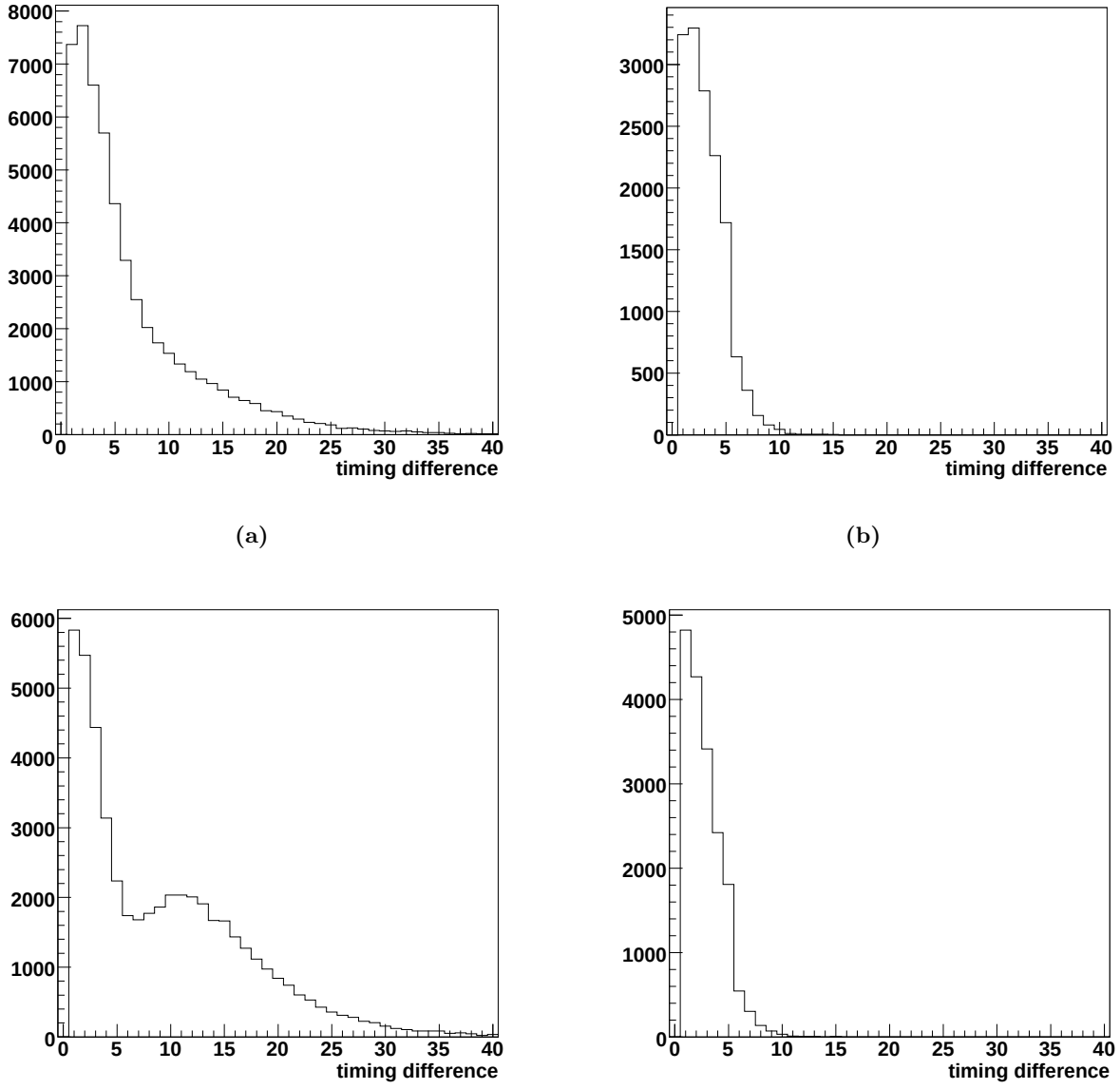

(a) **(b)**

(c) **(d)**

Figure 3.4: Distributions of number of multi pixel hits vs the time difference between adjacent pixels in clock cycles in helium 20% isobutane: (a) and (c) with a grid voltage of -420V and -440V respectively with no multi pixel hits removed; (b) and (d) With a grid voltage of -420V and -440V with all multi pixel hits with a time difference larger than 5 clock cycles between adjacent pixels removed. Multi pixel hits with zero time difference are not shown, as the tails become too small to see with such a large bin content in the first bin.

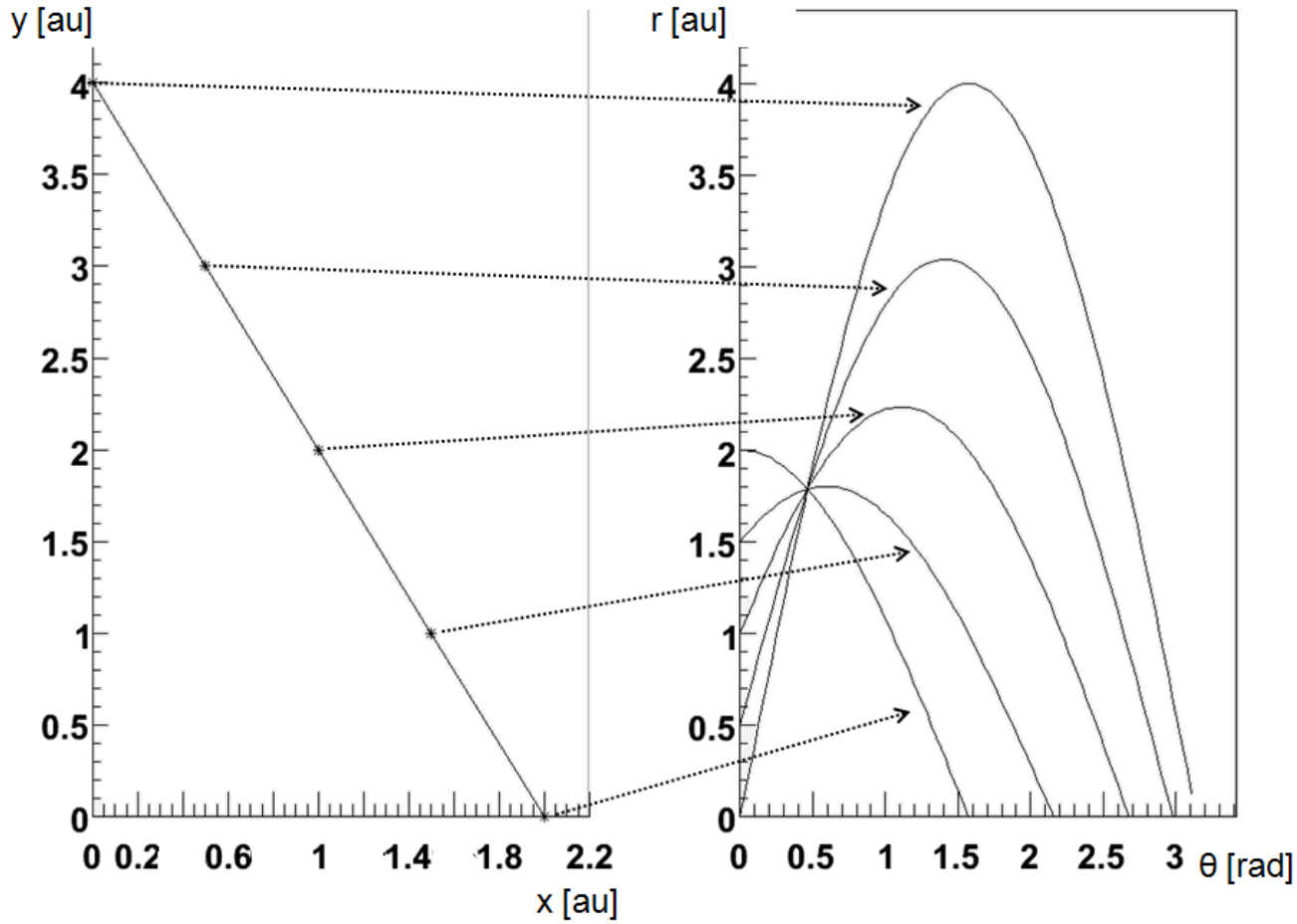

Figure 3.5: An example of a Hough Transformation of the straight line $y = 4 - 2x$ (left). The Hough Transformation is calculated for five points along the line. The curves in the (r, θ) plane intersect at the (r, θ) parametrisation of the line.

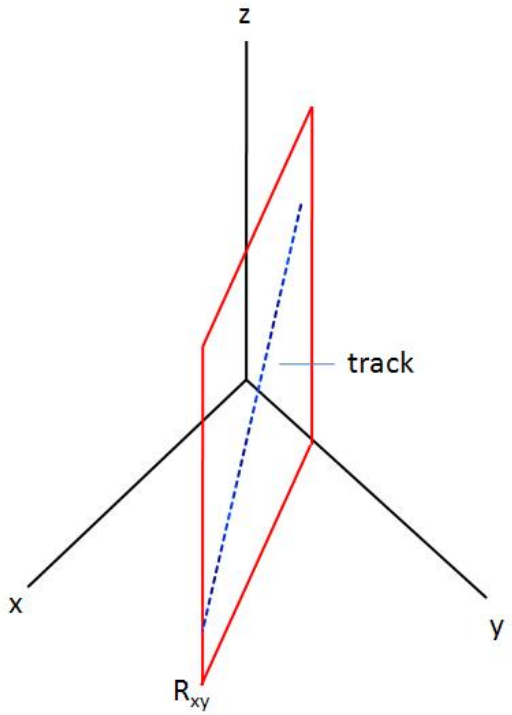

Figure 3.6: The choices of axes in this thesis. The R_{xy} axis is defined by the projected track, the dashed line, projected on the (x, y) plane.

than 20 assigned hits and 2.3 rad $< \theta <$ 2.7 rad were used.

In order to also exclude outliers in the z-direction, the procedure is repeated for the (R_{xy}, z) plane, only considering the selected hits for a track. The R_{xy}-axis is defined by the projected track of the particle in the (x, y) plane. See figure 3.6. $R_{xy} = 0$ at the intersection of the R_{xy} and y-axis. Once the track is found in (x, y), the R_{xy}-coordinate of each hit is calculated and the two-dimensional HT is repeated in R_{xy}/z. In this second step only one peak is expected in the (r, θ) histogram. This peak is found using the same process, only returning the largest peak. When a δ-ray is created, its track is probably more or less perpendicular to the track of the original fast particle and thus most likely rejected by the HT. All hits created by a δ-ray closer than three times the expected diffusion for that point to the fast particle's track are assigned to that track. In most cases around 95% of the raw hits are assigned to a track and thus used for fitting and almost 100% of all (multiple) tracks are found. The average numbers of hits assigned to a track for the different gas mixtures and grid voltages are summarised in table 3.2.

The choice for the HT for pattern recognition was a practical one. The method is widely used and therefore well tested, understood and described in literature. It is possible to also use a Hough Transform to find non-straight paths. This would be applicable when the fast particles are bent by a magnetic field. See[25] for an example of this.

gas	E_{drift} (V/cm)	-V_{grid} (V)	N_{hits}
Ar 3% CF_4 2% IsoBut	200	320	24
Ar 3% CF_4 2% IsoBut	200	340	50
Ar 3% CF_4 2% IsoBut	200	360	76
Ar 30% CO_2	470	430	21
Ar 30% CO_2	470	440	23
Ar 30% CO_2	470	460	50
Xe 30% CO_2	1000	490	102
Xe 30% CO_2	1400	440	63
Xe 30% CO_2	1900	460	101
Xe 30% CO_2	1900	465	121
Xe 30% CO_2	1900	470	132
He 20% IsoBut	560	400	52
He 20% IsoBut	560	420	57
He 20% IsoBut	560	440	62

Table 3.2: The average number of electrons assigned to a track for the different gas mixtures and grid voltages.

3.5 Track fitting

To fit the associated hits as returned by the HT, it is assumed that the track of the fast particle is a straight line. The fitting is done in two steps, firstly in the x/y-plane and secondly in the $R_{x,y}/z$-plane. In both planes, the errors in both directions are included in the fit. In this section the use of the χ^2 is exemplified, then the χ^2 fitting relevant for this research is explained and finally the testing of the fits is discussed.

The χ^2
With each data point (x_i, y_i) having its own, known standard deviation σ_i the most probable estimate of the model parameters $(a_0, ..., a_{M-1})$ describing the set (x_i, y_i) is found by minimising the quantity

$$\chi^2 \equiv \sum_{i=0}^{N-1} \left(\frac{y_i - y(x_i; a_0 ... a_{M-1})}{\sigma_i} \right)^2, \tag{3.4}$$

called the "chi-square". A rule of thumb is that a typical value for the χ^2 of a moderately good fit is $\chi^2 \approx \nu$, with $\nu = N - M$, the number of degrees of freedom. When fitting data to a straight line $y = a + bx$, the χ^2 becomes

$$\chi^2(a, b) = \sum_{i=0}^{N-1} \left(\frac{y_i - a - bx_i}{\sigma_i} \right)^2. \tag{3.5}$$

Suppose that theory predicts that our measured points are described by a polynomial function:

$$y_i^{theory} = \sum_{j=0}^{k-1} a_j \cdot (x_i)^j. \tag{3.6}$$

In vector form we write this as: $\vec{y}_{theory} = A\vec{\Theta}$ [26], where A is a matrix with n rows and k

columns, with n the number of measurements. And $\vec{\Theta}$ is a column vector with $(k+1)$ elements:

$$\vec{y}_{theory} = \begin{pmatrix} 1. & x_0 & x_0^2 & ... & x_0^{k-1} \\ 1. & x_1 & x_1^2 & ... & x_1^{k-1} \\ . & . & . & . & . \\ 1. & x_{n-1} & x_{n-1}^2 & ... & x_{n-1}^{k-1} \end{pmatrix} \begin{pmatrix} a_0 \\ a_1 \\ . \\ a_k \end{pmatrix}. \tag{3.7}$$

The χ^2 can then be written as:

$$\chi^2 = (\vec{y}_{exp} - A\vec{\Theta})^T G_y (\vec{y}_{exp} - A\vec{\Theta}), \tag{3.8}$$

where G_y is the inverse of the covariance matrix C_y. If the measurements are independent, this matrix is:

$$C_y = \begin{pmatrix} \sigma_0^2 & 0 & ... & 0 \\ 0 & \sigma_1^2 & ... & 0 \\ . & . & ... & \\ . & . & ... & \\ 0 & 0 & ... & \sigma_{n-1}^2 \end{pmatrix} \tag{3.9}$$

The best estimate for the unknown quantities $\vec{\Theta}$ is the one which minimises the χ^2. For these values:

$$\frac{d\chi^2}{d\vec{\Theta}} = -2A^T G_y (\vec{y}_{exp} - A\vec{\Theta}) = 0. \tag{3.10}$$

It follows that:

$$\vec{\Theta} = (A^T G_y A)^{-1} (A^T G_y \vec{y}_{exp}), \tag{3.11}$$

providing a very elegant numerical solution.
Minimising the χ^2 of a straight line the size of the total sum depends on the slope of the line: The error on the 'distance' $|y - a - bx|$ becomes larger with increasing b. This means that fitting becomes less accurate if $b > 1$. This effect has been compensated for in this thesis by reversing the x and y in the χ^2 if the slope b is larger than 1. This was the case in the x/y-plane for all beam test data.

The χ^2 with errors in both dimensions
When fitting the straight line model $y(x) = a + bx$, including errors in both directions, the χ^2 becomes [27]:

$$\chi^2(a,b) = \sum_{i=0}^{N-1} \frac{(y_i - a - bx_i)^2}{\sigma_{yi}^2 + b^2\sigma_{xi}^2} \tag{3.12}$$

where σ_{xi} and σ_{yi} are the standard deviations for the ith point, respectively. To understand this, we consider the variance of the linear combination $y_i - a - bx_i$ of two random variables x_i and y_i;

$$\mathrm{Var}(y_i - a - bx_i) = \mathrm{Var}(y_i) + b^2\mathrm{Var}(x_i) = \sigma_{yi}^2 + b^2\sigma_{xi}^2. \tag{3.13}$$

To find the minimum, we cannot use equation 3.11 as the χ^2 is no longer linear in the free parameters. Therefore the function minimiser Minuit2[28] used in ROOT [29] is used.
In order to fit the tracks in three dimensions, each track is fitted twice, once in the x/y-plane, and once in the R_{xy}/z-plane. If all three dimensions were to be fitted in once, it would be increasingly complicated to include errors in all dimensions.

Including errors
In the x/y-plane the expected error of every hit is the same in both directions. The expected

error is the expected point resolution of the detector plus the expected transverse diffusion as derived by MAGBOLTZ. In the $R_{x,y}/z$-plane the expected error in the $R_{x,y}$ direction is the error for that point from the previous fit plus its expected transverse diffusion. In the z-direction the expected error is calculated from the expected longitudinal diffusion and the zero point resolution in that direction.

Testing the fits
To test the goodness-of-fit, two characteristics of the fit are examined. Firstly the χ^2 distribution for n degrees of freedom is calculated as

$$f(z;n) = \frac{z^{n/2-1}e^{-z/2}}{2^{n/2}\Gamma(n/2)}. \tag{3.14}$$

For large n, the χ^2 distribution approaches a Gaussian with mean $\mu = n$ and variance $\sigma^2 = 2n$. Assuming the goodness-of-fit statistic follows a χ^2 distribution, the χ^2 probability p is then

$$p = \int_{\chi^2}^{\infty} f(z;n)dz. \tag{3.15}$$

Experimentalists are often rather tolerant to low probabilities p. It is not uncommon to accept a model with a $p > 0.001$. This lower bound is also used in this thesis. Please find more information on the use of the χ^2 probability function in [27].
For the second goodness-of-fit test the *pull* is used:

$$\text{pull} = \frac{r_i}{\sigma_i}, \tag{3.16}$$

where r_i of each hit is defined as the distance between its measured position and its projected position on the track. The pull distribution should be a gaussian distribution around zero with a standard deviation of one. If the standard deviation is larger than one, the error is underestimated, if the standard deviation is smaller than one, the error is overestimated. If the distribution is not centered around zero, the model does not accurately describe the data. In our case this might indicate that the tracks are not actually a straight line.

3.6 Reconstructing the spatial resolution

To investigate the spatial resolution of the detector, the xy-plane and z-direction are treated separately. The residuals distribution is affected different ways:

- by the transverse diffusion, causing the electrons to be gaussian distributed around the point of creation in the perpendicular direction to the drift;
- the range of the primary electrons, although a HT is performed, the hits created by δ-rays closer than three times the expected diffusion to the tracks are assigned to the track, affecting the residual distribution;
- if the multi pixel hits are not removed, they are introduced in the analysis as normal hits and thus alter the distribution;
- electric drift field distortions may affect the drift velocity and projected location of the drifting electrons;

- due to time slewing, electrons appear to arrive later;
- possible other influences.

The effect of the diffusion on the spatial resolution is further investigated by reconstructing the measured diffusion. In the x/y-plane the total variance of the residuals is expected to be a combination of the zero point resolution, $\sigma_{xy,0}$ and the diffusion in the transverse direction D_t. As seen in section 2.5, the variance of the residuals due to diffusion is

$$\sigma_t^2 = D_t^2 \cdot z. \tag{3.17}$$

The zero point resolution is calculated by assuming that the hits are distributed uniformly over each pixel and is thus determined by the variance of the random distribution:

$$\sigma_{xy,0} = \delta x/\sqrt{12}. \tag{3.18}$$

Because the GridPix' pixel size is 55μm, a point resolution of 16μm for zero diffusion is expected. Because the two variances are uncorrelated, they can be added quadratically:

$$\sigma_{xy}^2(z) = \delta x^2/12 + D_t^2 \cdot z. \tag{3.19}$$

To measure $\sigma_{xy,0}$ and D_t, the square of the residuals is plotted as a function of z and fitted with a linear function. The expected transverse diffusion coefficients as calculated with MAGBOLTZ are listed in table 8.2.
In the R_{xy}/z-plane the distribution of the residuals is altered by the same effects as the distribution in the x/y-plane, but the best point resolution is limited by the clock frequency. With clock cycles of 10 ns and e.g. a drift velocity of 2.1 cm/μsec in helium 20% isobutane, a resolution of $210/\sqrt{12} = 61\mu$m is expected.

3.7 Reconstructing number of clusters per cm

One of the means to identify charged particles is through their energy loss in the drift volume. This energy loss can be determined by measuring the number of clusters per unit length along the track. To be able to identify clusters meaningfully, the electron diffusion should be taken into account. To identify clusters all hits are projected on the track, if the distance between projections is smaller than the measured transverse diffusion for that point, the hits are grouped in a cluster. The centre-of-gravity of every cluster is projected on the track to find the reconstructed point of creation.
The distribution of the distances l between successive clusters is expected to be a decreasing exponential function:

$$f(l) = p_0 e^{-p_1 l}, \tag{3.20}$$

where p_1 is an estimate of the number of clusters per unit length along the track. The expected number of clusters per cm depends on the gas mixture, temperature, gas pressure, the identity and momentum of the traversing particle. For this thesis room temperature and standard pressure are assumed. To calculate the expected number of clusters per cm of track, numbers from [7] are used. The relevant expected values for the number of clusters per cm are given in table 4.4.

Chapter 4

Results and discussion

In this chapter the results of the analysis are presented and discussed. The results from data obtained at Nikhef are discussed separately from the beam test data. In the next sections the goodness of fit tests are explained, the diffusion and zero point resolution measurements are discussed and the analysis of energy loss is presented.

4.1 Drift velocity

In figure 4.1 the clock cycle distributions of 6 different runs are shown. The measured values for the drift velocities are listed in table 4.1. These values, except when using the gas mixture argon 3% CF_4 2% isobutane, are in good agreement with expected values from MAGBOLTZ. In all results presented in this thesis, the derived values for the drift velocities are used in the calculations.

4.2 Testing goodness-of-fit

To illustrate the two goodness-of-fit tests as performed for all fitted data samples, the data samples of run 02030102 and 02030103 in helium 20% isobutane are chosen. These runs with 3575 and 1053 triggers respectively were performed with the beam traversing the drift volume parallel to the chip on approximately 1 cm from the chip, an electric drift field of 560 V/cm, -420 V and -440 V on the grid respectively and particle identification for both electrons and pions. These runs will be used throughout this chapter to illustrate the different analysis steps. For the purpose of this section, the differences in the pull and χ^2 probability distributions for the first 1000 events from each data sample are discussed with and without the exclusion of the multi pixel hits.

gas	E_{drift} (V/cm)	v_{drift} exp (cm/μsec)	v_{drift} measured (cm/μsec)
Ar 3% CF_4 2% IsoBut	200	7.5	4.3 ± 0.4
Ar 30% CO_2	470	1.2	1.2 ± 0.1
Xe 30% CO_2	1000 / 1400 /1900	1.9 / 3.5 / 5	1.9 ± 0.2 / 3.4 ± 0.3 / 4.9 ± 0.5
He 20% IsoBut	560	2.1	2.2 ± 0.2
Ar 20% IsoBut	600	4.3	4.4 ± 0.4

Table 4.1: Expected and measured drift velocities in the different gas mixtures used.

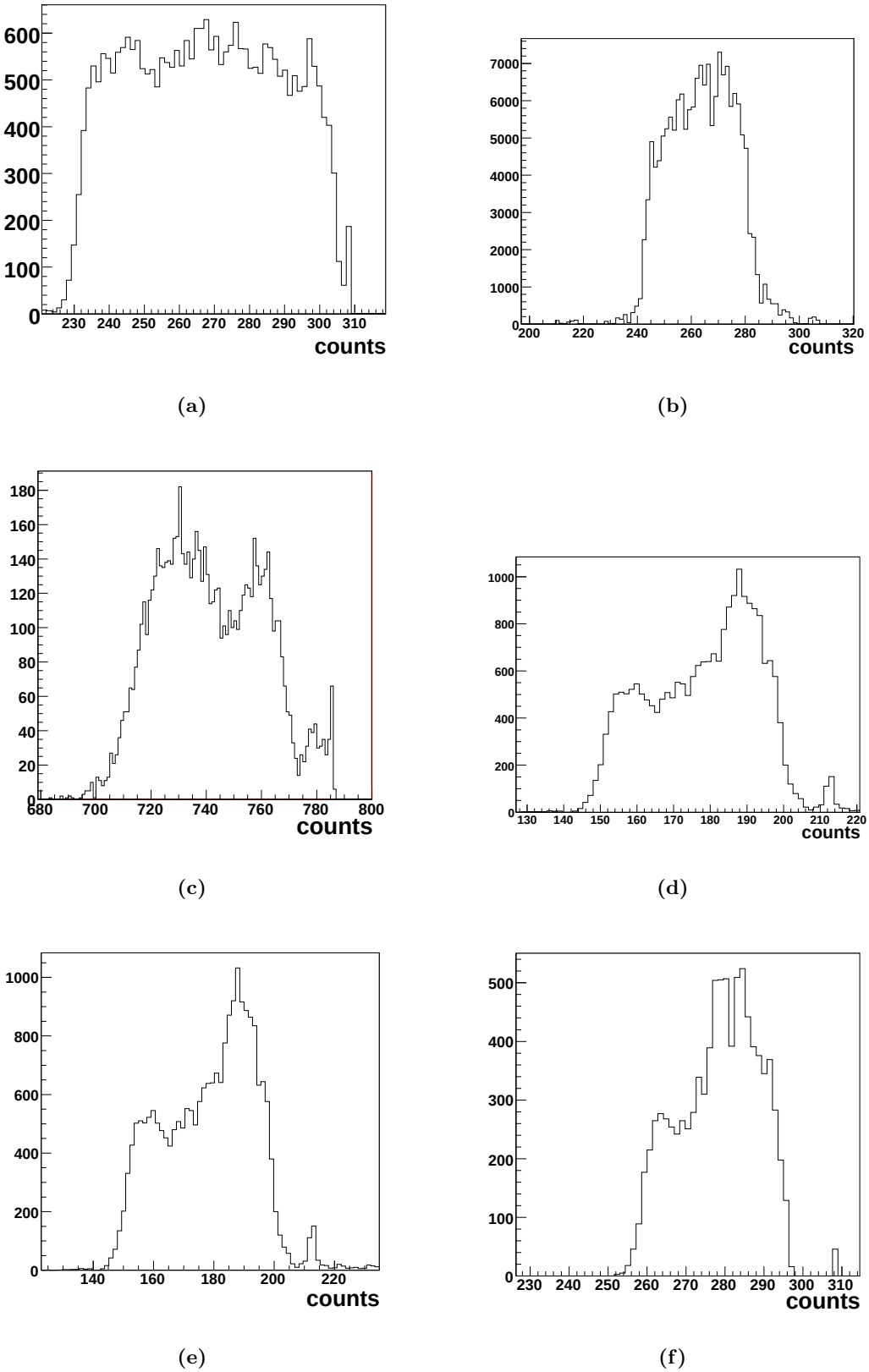

Figure 4.1: Distributions of clock cycles for 5 runs from the beam test, and one (c) of the magnet data. In (a) we see the distribution of helium 20% isobutane with $E_{drift} = 560$ V/cm, the detector was placed under a 25° angle with respect to the beam, so that the whole 17 mm drift was used. (b) shows argon 3% CF_4 2% isobutane with $E_{drift} = 200$ V/cm also with a 25° angle with respect to the beam. (c) is of magnet data using argon 20% isobutane with $E_{drift} = 600$ V/cm and a drift length of 29 mm. (d) is of xenon 30% CO_2 with $E_{drift} = 1000$ V/cm and with the anode parallel with respect to the beam, reducing the maximum drift length to 10 mm, the size of the second scintillator. (e) and (f) are in xenon 30% CO_2 with $E_{drift} = 1400$ and 1900 V/cm respectively and under an angle.

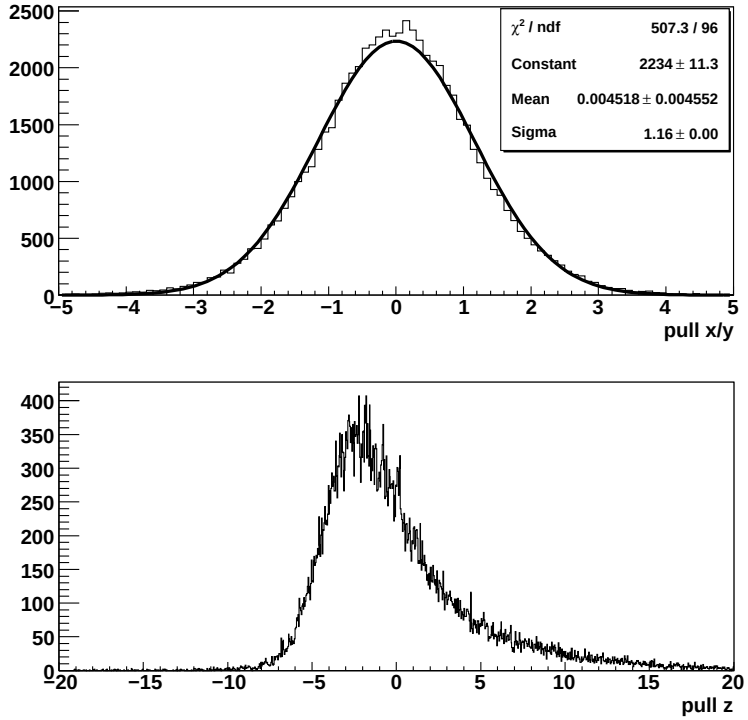

(a)

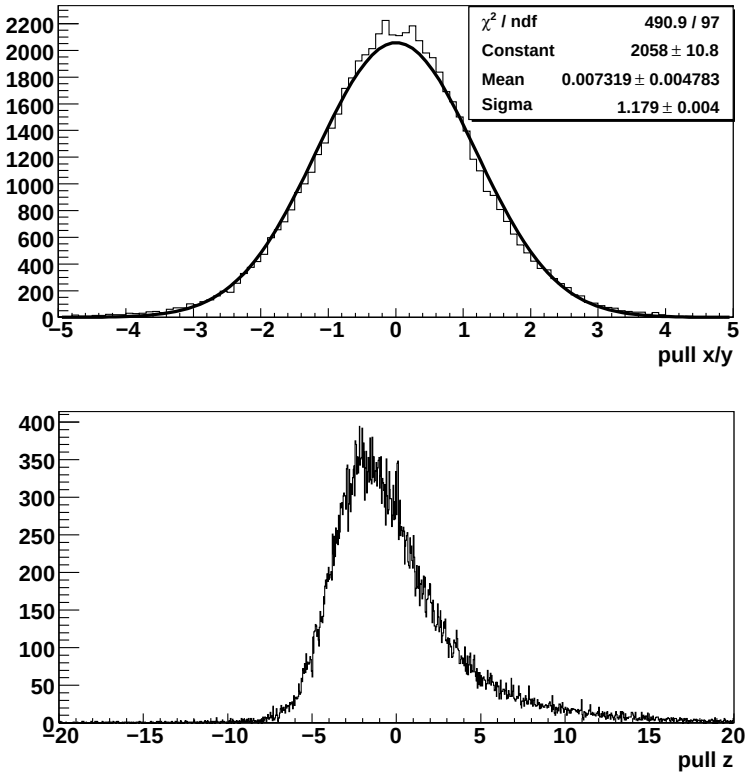

(b)

Figure 4.2: The pull distributions in x/y and R_{xy}/z without (a) and with (b)the exclusion of multi pixel hits of the first 1000 triggers of run 02030102, with a grid voltage of -420V.

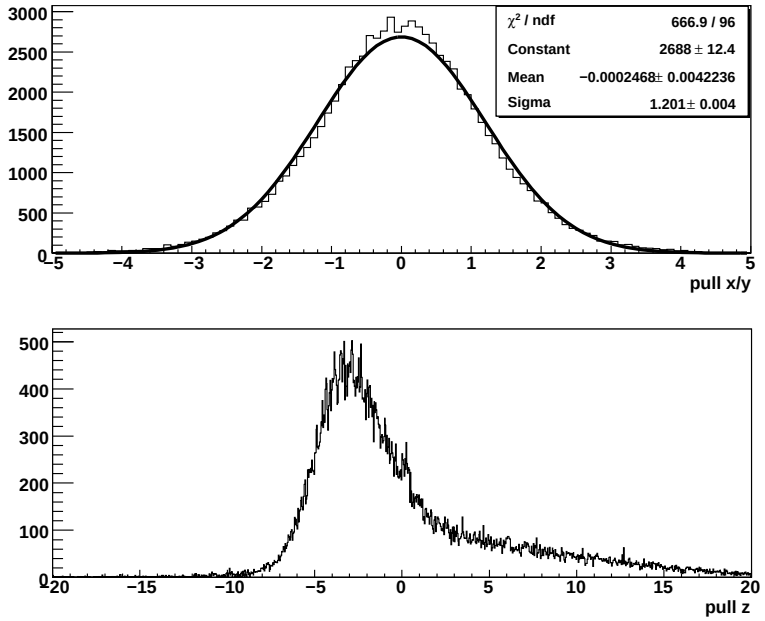

(a)

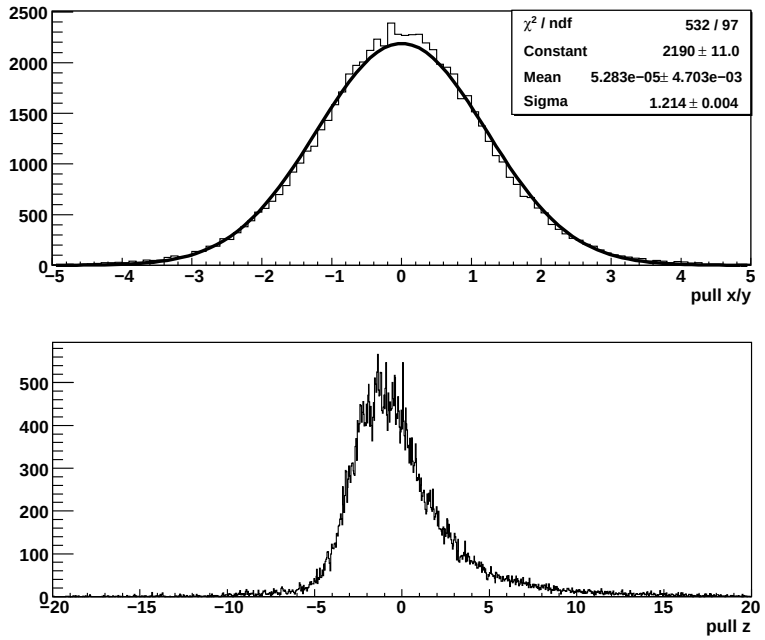

(b)

Figure 4.3: The pull distributions in x/y and R_{xy}/z without (a) and with (b)the exclusion of multi pixel hits of the first 1000 triggers of run 02030103, with a grid voltage of -440V.

Pull
The pull distributions for all fitted runs are checked after fitting. As an example the pull distributions for the first 1000 triggers of run 02030102 and 02030103 are displayed in figures 4.2 and 4.3. In all cases the mean of the distributions is between -0.01 and 0.01, indicating that the fitted tracks are on average in the middle of the data cloud. In the (x, y) plane, the distributions are symmetrical around zero. In the z-direction the distributions are not centered around zero, which indicates that the residuals are not accurately measured. As there are more pulls with a positive value, meaning that the z-coordinate of the projected hit is larger than the coordinate of the original hit, this is probably caused by time slewing. When comparing pull distributions of run 02030103, with a grid voltage of -440V, it is seen that the distribution becomes less asymmetrical when the multi pixel hits are removed. This indicates that the reconstruction of the residuals in the z-direction improves when the multi pixel hits are taken out of the data before fitting. This effect is much smaller for run 02030102, with a grid voltage of -420V.

To test the error estimation a gaussian function is fitted to the pull distributions in the (x, y) plane. The standard deviation of these gaussian functions is around 1.2 for all shown data sets. This indicates that the error included in the fit underestimates the real error slightly. This is probably caused by the fact that the error is estimated from the expected diffusion from MAGBOLTZ.

χ^2 probability
The χ^2 and χ^2 probability distributions of the first 1000 files of run 02030102 and 02030103 with and without the exclusion of the multi pixel hits are displayed in figure 4.4 and 4.5. The χ^2 are divided by ν, so their values should be roughly one. All the depicted χ^2 values are close enough to one to be satisfactory. When looking at the χ^2 probabilities for run 02030103 we find that the number of fits with a $p < 0.1$ in the R_{xy}/z-plane decreases from 558 to 195 when the multi pixel hits are removed. The removal of the multi pixel hits for run 02030102 does not seem to have such an effect. If the χ^2 probability is too close to one, too good to be true, the error is most probably overestimated, this is the case for clean tracks produced close to the chip. For the remainder of this thesis only fits are used for which the χ^2 probability in both dimensions is larger than 0.001. The fits with very small p are usually very "blobbed" when checked with the Pixelman viewer.

4.3 Diffusion

To measure the transverse diffusion, the residuals are plotted as a function of their reconstructed z, see figure 4.6. The variance of the residuals at a given z is calculated by dividing the histogram in slices of $\Delta z = 1$ along the z-axis. The residuals in these slices are measured from hits with similar drift lengths. A gaussian function is fitted to the one-dimensional histogram of each slice. The standard deviation of this gaussian function is interpreted as the variance of the residual for that given z. When plotting the square of these standard deviations as a function of z, we recognise a linear dependence, as expected from 3.19. Because the time difference between the coincidence of the trigger and gate opening is only 13 ns, comparable to the duration of one count, it is neglected and it is assumed that the hits with the highest count were created with zero drift. When a straight line is fitted through the points, the slope of that line can be interpreted as D_t^2 in pixel^2/count. At zero drift, the zero point resolution in pixel^2 can be extracted. To calculate the diffusion in $\mu\text{m}/\sqrt{\text{cm}}$ the drift velocity in cm/count is used.

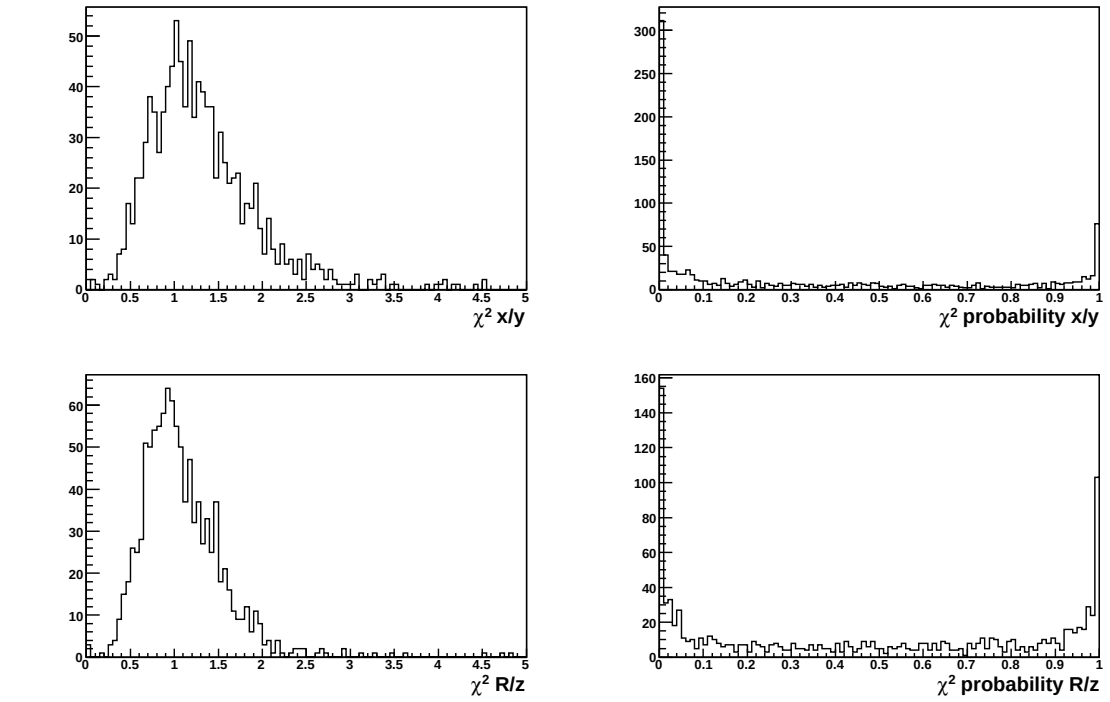

(a)

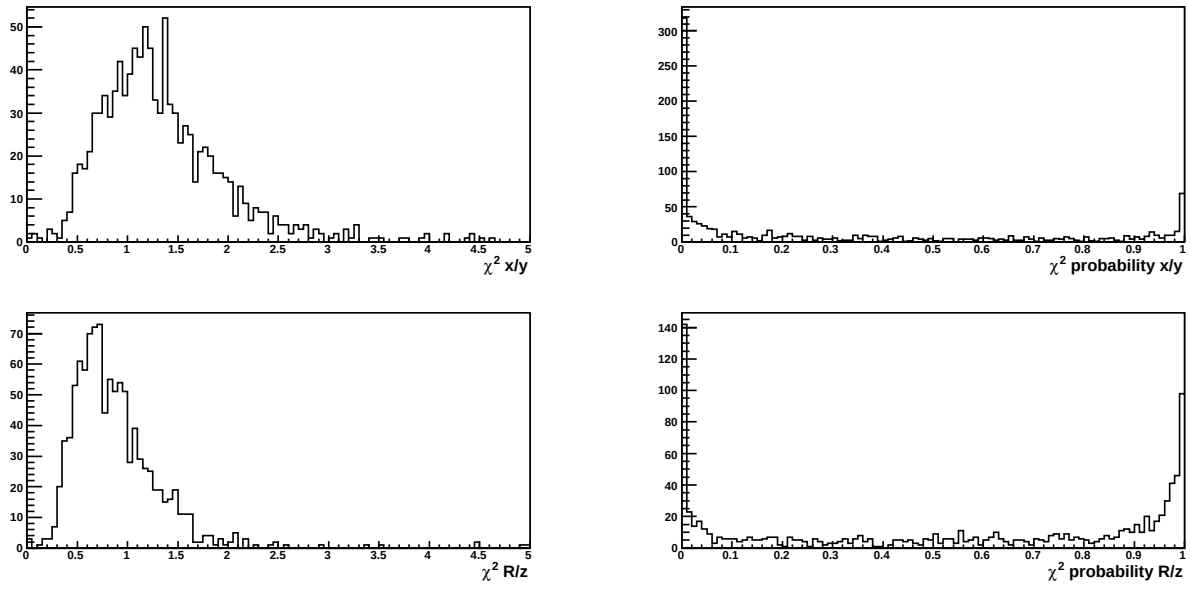

(b)

Figure 4.4: The χ^2 and χ^2 probability distributions without (a) and with (b) the exclusion of multipixel hits of the first 1000 triggers of run 02030102, with a grid voltage of -420V.

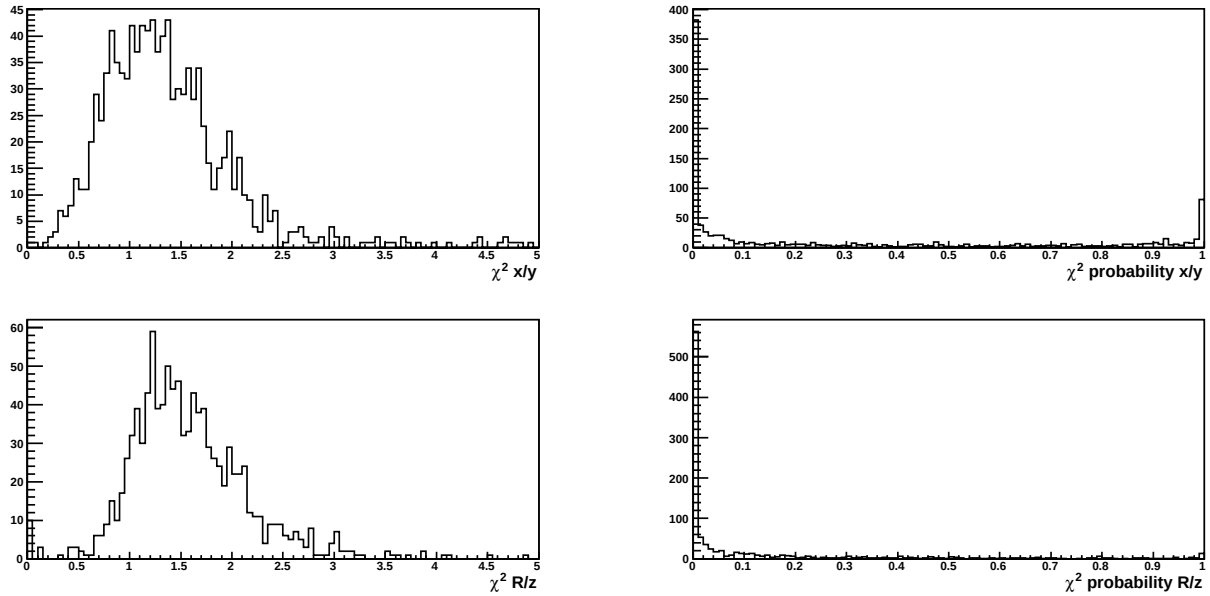

(a)

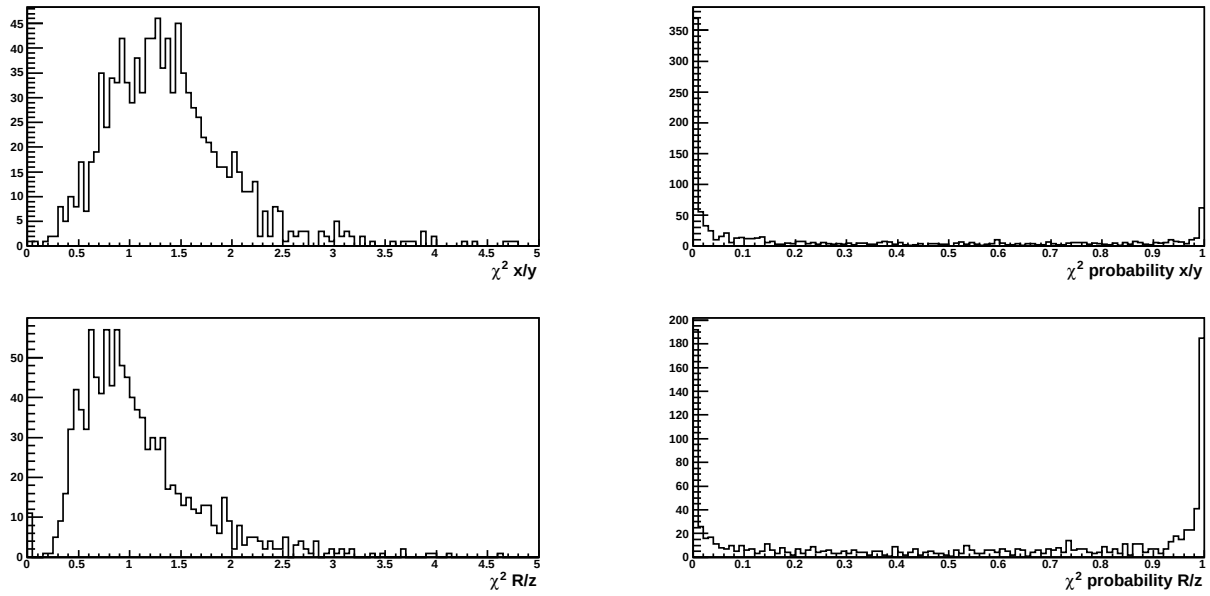

(b)

Figure 4.5: The χ^2 and χ^2 probability distributions without (a) and with (b) the exclusion of multipixel hits of the first 1000 triggers of run 02030103, with a grid voltage of -440V.

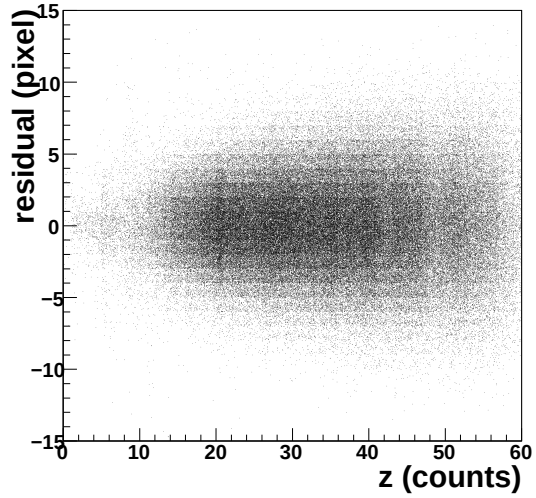

(a)

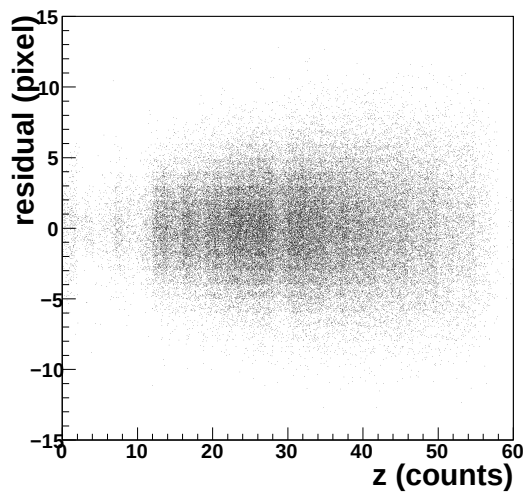

(b)

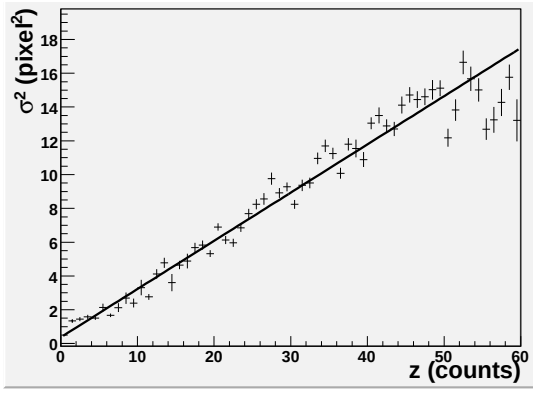

(c)

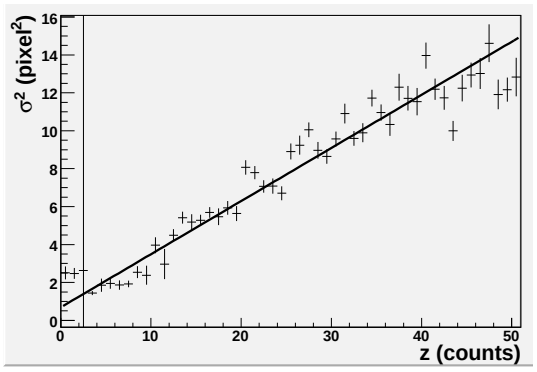

(d)

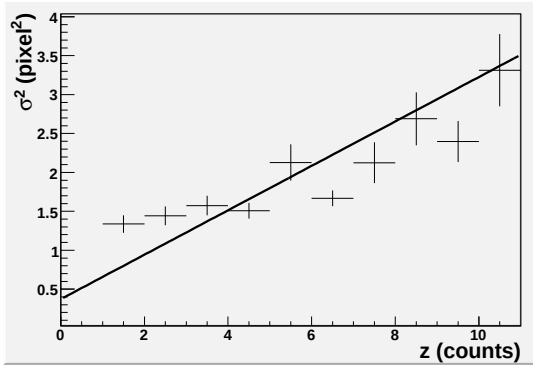

(e)

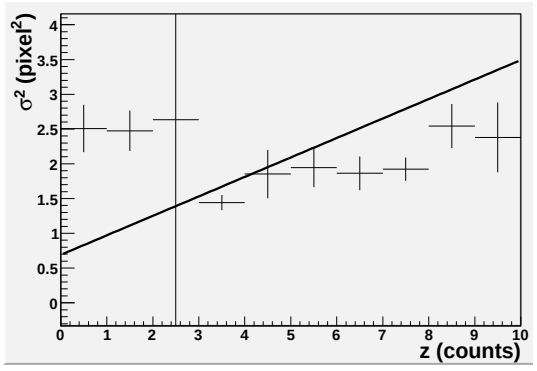

(f)

Figure 4.6: The two-dimensional histograms of the residuals as a function of the reconstructed z of run 02030102 (a) and 02030103 (b). The two-dimensional histograms are divided into slices, each slice contains a one-dimensional histogram which is fitted with a gaussian function. The variances of these gaussians are plotted in (c) and (d) respectively. In (e) and (f), we zoom in on the first 10 bins of (c) and (d). The large error in the third bin of (d) and (f) is due to small statistics or some outliers in this bin in (b).

gas	E_{drift} (V/cm)	D_t exp ($\mu m/\sqrt{cm}$)	D_t measured ($\mu m/\sqrt{cm}$)	$\sigma_{xy,0}$ (μm)
Ar 3% CF_4 2% IsoBut	200	290	138 ± 2.5	35±11
Ar 30% CO_2	470	148	80 ± 2	24±7
Xe 30% CO_2	1000	185	40 ± 8	30±15
Xe 30% CO_2	1400	103	134 ± 3	23±11
Xe 30% CO_2	1900	110	171 ± 4	17±14
He 20% IsoBut	560	175	176 ± 2	27±14

Table 4.2: Expected and measured diffusion for combined test beam runs.

4.3.1 Beam test data

In table 8.2 all measured values of the transverse diffusion and zero point resolution in the beam test are listed. As mentioned in section 2.5 the transverse diffusion only depends on density and mixture of the gas and the strength of the electric drift field. In table 4.2 all combined reconstructed transverse diffusions and zero point resolutions using all comparable runs are listed. Here the results are discussed per gas mixture.

Transverse diffusion

- As a proof of principle the reconstructed transverse diffusion in helium 20 % isobutane is first examined. With all measurements combined, the reconstructed transverse diffusion is 176 ± 2$\mu m/\sqrt{cm}$, which is in good agreement with the MAGBOLTZ prediction of 175$\mu m/\sqrt{cm}$.

- For argon 3% CF_4 2% isobutane the measured value of 138 ± 4 $\mu m/\sqrt{cm}$ differs a factor 2.1 from the expected value of 290 $\mu m/\sqrt{cm}$, this difference was expected because the measured value for the drift velocity, 4.3 cm/μsec differs by a factor 1.7 from the expected value of 7.5 cm/μsec.

- In argon 30% CO_2 the total measured diffusion is calculated excluding run 01020302 and run 01020304. These runs were taken with different coincidence characteristics, reducing the maximum drift length to approximately 0.3 cm. With a maximum drift length of 0.3 cm, there are only about 4 slices of Δz, which is not enough to measure the slope of the fitted line. The combined transverse diffusion is 80 ± 2 $\mu m/\sqrt{cm}$. The expected value is 148 $\mu m/\sqrt{cm}$. This difference cannot be assigned to a difference in expected and measured drift velocity. A possible explanation for this difference is that these measurements were taken with the second coincidence scintillator in rather low position with respect to the chip. Therefore I am not sure if the whole 17 mm drift space was used. If not, the drift velocity is not well measured again altering the reconstructed diffusion.

- When turning attention to the measurements with xenon 30% CO_2, we need to separate the measurements with different electrical drift fields, as these yield different diffusions. One measurement of 775 events is done with a drift field of 1000 V/cm. The expected diffusion is 185 $\mu m/\sqrt{cm}$, whereas the reconstructed value is 40 ± 8 $\mu m/\sqrt{cm}$. For a drift field of 1400 V/cm the expected diffusion is 103 $\mu m/\sqrt{cm}$, whereas the reconstructed value is 134 ± 3 $\mu m/\sqrt{cm}$. With the drift field set to 1900 V/cm we expect 110 $\mu m/\sqrt{cm}$ and measure 171 ± 4 $\mu m/\sqrt{cm}$. These results are not consistent with calculations from MAGBOLTZ, moreover the behaviour when comparing to MAGBOLTZ is different. From calculations, the transverse diffusion is expected to decrease significantly when increasing

gas	B field (T)	D_t expected (μm/$\sqrt{\text{cm}}$)	D_t measured (μm/$\sqrt{\text{cm}}$)
He 23% IsoBut	0	180	175 ± 5
He 23% IsoBut	0.5	176	170 ± 6
He 23% IsoBut	1	170	168 ± 5
Ar 20% IsoBut	0	160	164 ± 4
Ar 20% IsoBut	0.5	155	199 ± 10
Ar 20% IsoBut	1	153	159 ± 4
Ar 3% CF_4 2% IsoBut	0	290	144 ± 6
Ar 3% CF_4 2% IsoBut	0.5	148	127 ± 6
Ar 3% CF_4 2% IsoBut	1	90	106 ± 7

Table 4.3: Expected and measured diffusion for all combined runs performed with the magnet at Nikhef.

the strength of the electrical drift field. From measurements we see that the transverse diffusion increases with increasing drift field.

Zero point resolution, $\sigma_{xy,0}$
In table 4.2 the measured zero point resolutions are summarised. The zero point resolution should not depend on gas mixture or electric drift field, so all measurements can be combined to find a measured value of 26±12 μm , whereas 16 μm is expected. The error for all measured points is calculated with the estimation that the position of the fitted line could be translated along the z-axis with $\pm 1/\sqrt{12}$, the zero point resolution in z. Then the intersection with the y-axis will shift $\pm D_t^2/\sqrt{12}$. This is the error stated in the table. There are two reasons why this reconstructed value does not compare to the expected value. Firstly, the zero point resolution depends only on the location of the fitted line with respect to the y-axis. The determination of this location performed for this research is very error prone, due to the fact that we are not exactly sure what number to use for z_{max} in equation 3.1. When using the raw data, the number for z_{max} can differ from event to event by up to six counts and is influenced by time slewing effects. Therefore the error on the measured zero point resolutions is probably bigger than the error stated. Secondly, it is questionable that the intersection with the y-axis of the (extrapolation of the) fit is a good measure of the zero point resolution. When zooming in on the first ten bins of the fitted variances, as seen in figure 4.6 (e) and (f), we see that the data points in all cases are above the fitted line. Thus the true zero point resolution is probably larger than the reconstructed one. This could be caused by the fact that the electrons are emitted perpendicular to the track. If the distance travelled by the emitted electrons becomes of order of the diffusion or larger, which is the case at small or no drift, the extrapolation of the line is not a good measure for the zero point resolution.

4.3.2 Inclusion of magnetic field

Transverse diffusion
In table 4.3, the measured transverse diffusion for all runs taken at Nikhef with different magnetic fields are shown.

- When using helium 23% isobutane, the measured coefficients are in good agreement with the expected values. The transverse diffusion decreases only slightly under the influence of the magnetic field, as expected.

- In argon 20% isobutane the measurement performed with a magnetic field of 0.5 T only produced 25 usable tracks during measurements. The transverse diffusions found in a

magnetic field of 0 and 1 T are in agreement with MAGBOLTZ and again the decrease in diffusion is small.

- For argon 3% CF_4 2% isobutane the transverse diffusion decreases from 144 ± 6 $\mu m/\sqrt{cm}$ without magnetic field to 106 ± 7 $\mu m/\sqrt{cm}$ with a magnetic field of 1 T and is just significant. This was also expected from equation 2.8 as the mean free path between collisions, λ_e, and thus τ_e, is quite large compared to the other gases used. All measured values differ from the expected values as the measured drift velocity was not in agreement with the expected velocity, providing a difficulty comparing these values.

Zero point resolution, $\sigma_{xy,0}$
To find the zero point resolution in this case, we need to take the delay between coincidence and gate opening into account. If the delay is not taken into account, electrons that have drifted some distance during the delay, are measured to have zero drift. As this delay has not been accurately measured, a 100 ns delay is estimated. When the reconstructed values for z are compensated for the delay, some of measured zero point resolutions yield unphysical negative values. Without a better estimate of the delay, the zero point resolution can not be reconstructed any better.

4.4 Number of clusters per unit length

To measure the number of clusters per cm of track length, a plot is made of the distance between all successive clusters along the tracks. See figure 4.7 for an example of such a plot, from the events of run 02030105. The distribution is fitted with a decreasing exponential function (equation 3.20). Only events from runs with particle identification are used for this part of the analysis. In this way we can check if it is possible to distinguish electrons from pions in the data from the GridPix detector. The reconstructed values of number of clusters per cm for electrons and pions with this method are listed in tables 8.3 and 4.4. The error on the average values becomes of the order of $\frac{\sqrt{N}}{\sqrt{M}}$, with N the number of clusters per cm and M the number of events used. This is the error stated in table 4.4. If the number of clusters is measured using one track, the error is of order $\sqrt{N}$. In the ILC's experiment the tracks will be of 1.2 m track length, this could allow particle identification using one track.

Using this procedure, the error on the number of clusters per cm can become infinitesimally small when M becomes large. This is not very useful, because in experiments each fast particle's identity needs to be identified. Therefore the number of clusters is also counted for each cm track.

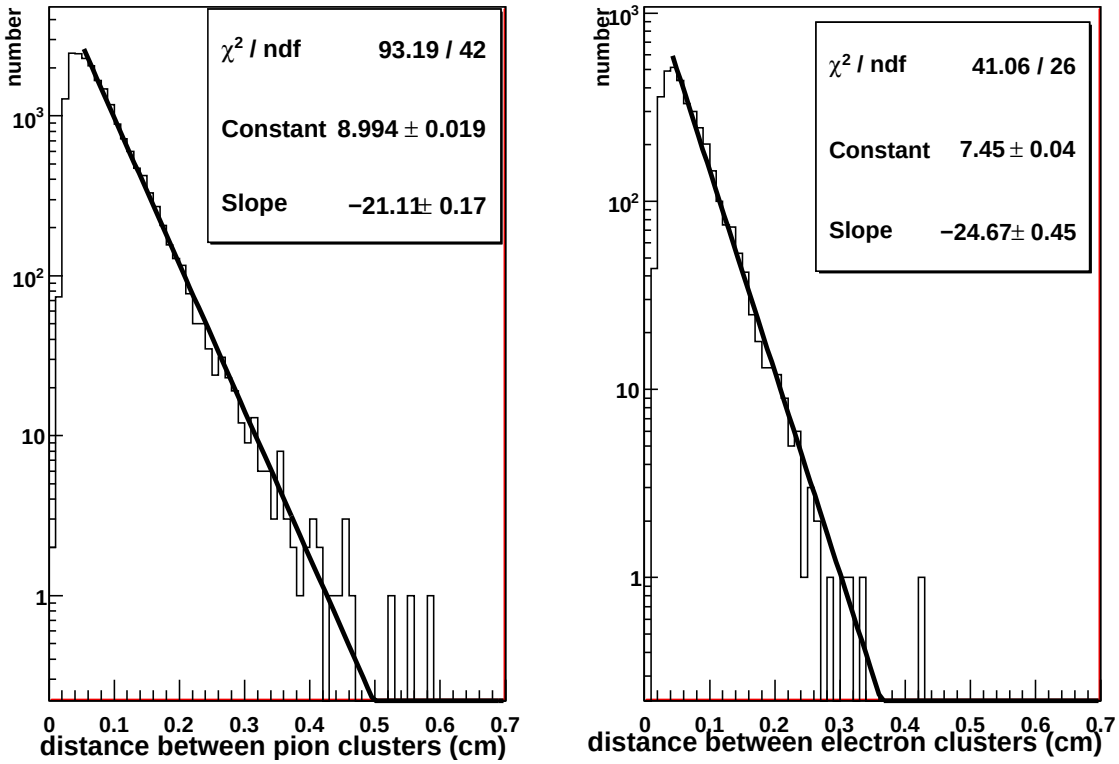

Figure 4.7: The distance between the projected positions of successive clusters of pion (left) and electron (right) tracks. The y-axis is set to a log scale. The number of clusters per cm of track length can be found by fitting a decreasing exponential function to the distribution. The slope of this function is a measure for the number of clusters per cm of track length.

gas	particle	n_p/cm expected	n_p/cm measured
Ar 3% CF_4 2% IsoBut	elec	22.2	22.6 ± 1.6
Ar 3% CF_4 2% IsoBut	pi	18.2	18.6 ± 1.4
Xe 30% CO_2	elec	16.7	11.8 ± 0.4
Xe 30% CO_2	pi	14.7	7.7 ± 0.2
He 20% IsoBut	elec	24.9	26.37 ± 0.09
He 20% IsoBut	pi	21.9	20.90 ± 0.05

Table 4.4: Expected and measured number of clusters per cm track for all test beam runs combined.

In figure 4.8, the number of clusters per cm is shown in helium 20% isobutane and in figure 4.9 for xenon 30% CO_2. The number of clusters measured for electrons is 27 with an RMS of 6 and for pions 21 with an RMS of 5 in helium 20% isobutane. Clearly, the errors are too large with one cm track length. When combining different tracks to one track of 25 cm length, the error should become smaller. The number of clusters per cm measured for 25 cm of track is shown in figures 4.8 (b) for helium and 4.9 (b) for xenon. The RMS on the number of clusters per cm in helium is now reduced to 1.2 for electrons and pions. The difference between these numbers becomes:

$$n_e - n_\pi = (28.4 \pm 1.2) - (21.0 \pm 1.2) = 7.4 \pm 1.7, \tag{4.1}$$

so with 25 cm of track length electrons and pions can be distinguished with a confidence level of 4.4σ.

In xenon we find that the RMS on the measured values of number of clusters per cm track length is reduced from 4.0 to 1.0 for electrons and from 5.8 to 1.8 for pions using 25 cm of track, so:

$$n_e - n_\pi = (18.6 \pm 1.0) - (12.5 \pm 1.8) = 6.1 \pm 2.1, \tag{4.2}$$

enabling distinction between electrons and pions with a confidence level of 2.9σ.

The cluster counting method eliminates the Landau fluctuations in the number of electrons per primary ionisation cluster. This can be illustrated by counting the total number of single electrons per unit of track length, instead of the number of clusters. These distributions, again for the gas mixtures helium 20% isobutane and xenon 30% CO_2 are shown in figures 4.10 and 4.11, both for single ($\approx$ 1 cm) tracks and the 25 cm combined tracks. One can clearly observe the long high-end tails in these distributions. Using 25 cm of track length, the number of single electrons per cm is 46.0 with an RMS of 5.1 for electron and 41.5 with an RMS of 5.1 for pions. For xenon 30% CO_2 we find 151 with an RMS 49 for electrons and 131 with an RMS of 42 for pions. This does not allow a distinction between electrons and pions.

In this last part of the analysis the measurements with particle identification in argon 3% CF_4 2% isobutane are not taken into account, as there was only one 25 cm track for electrons in this gas.

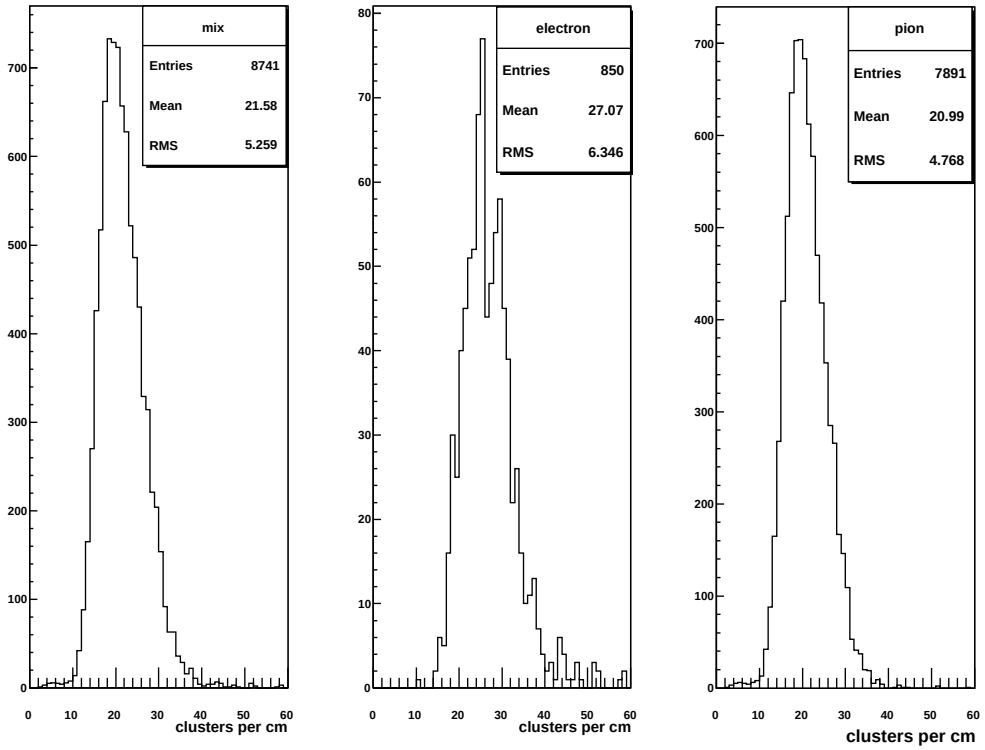

(a)

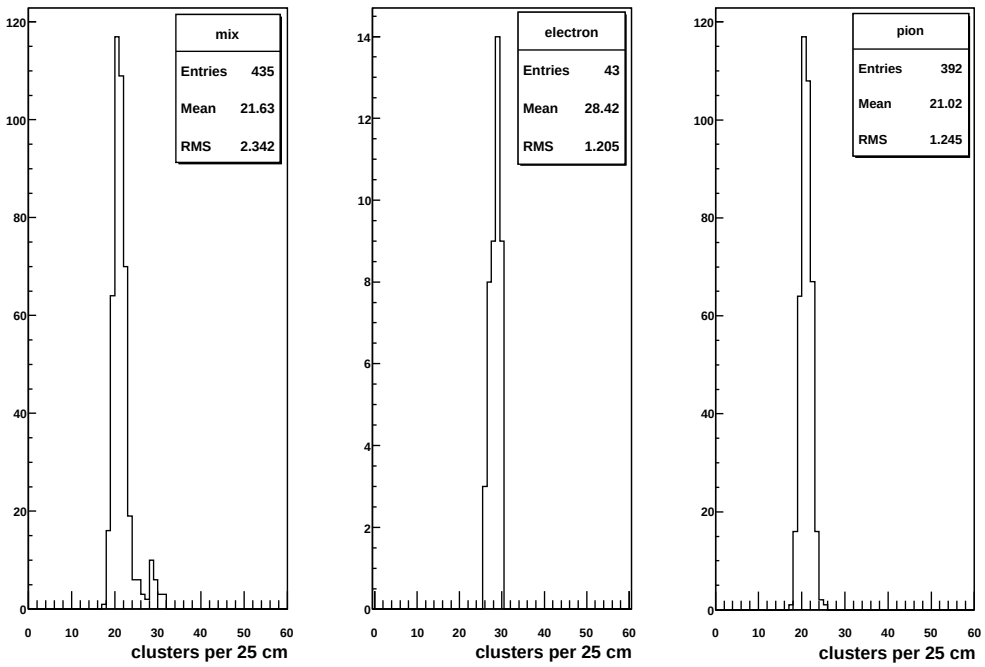

Figure 4.8: The number of clusters per cm in helium 20% isobutane, calculated for each cm track (a) and for 25 cm of track (b). The double peak in the histogram for the electrons dissapears if run 0203101, 02030102 and 02030103 are left out of the calculation. These runs were taken on a different day than the other runs, which could mean that the pressure in the chamber was different due to weather conditions. It is unexpected that the different peaks do not show up in the pion histogram. This is not investigated any further.

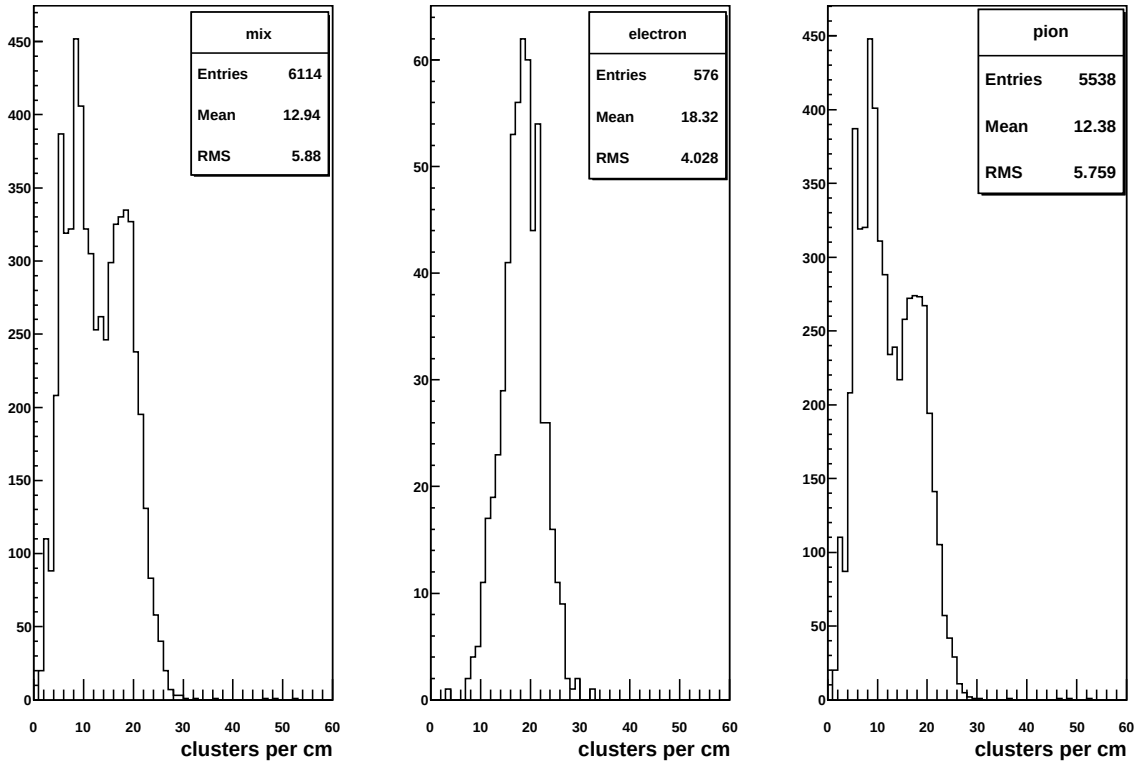

(a)

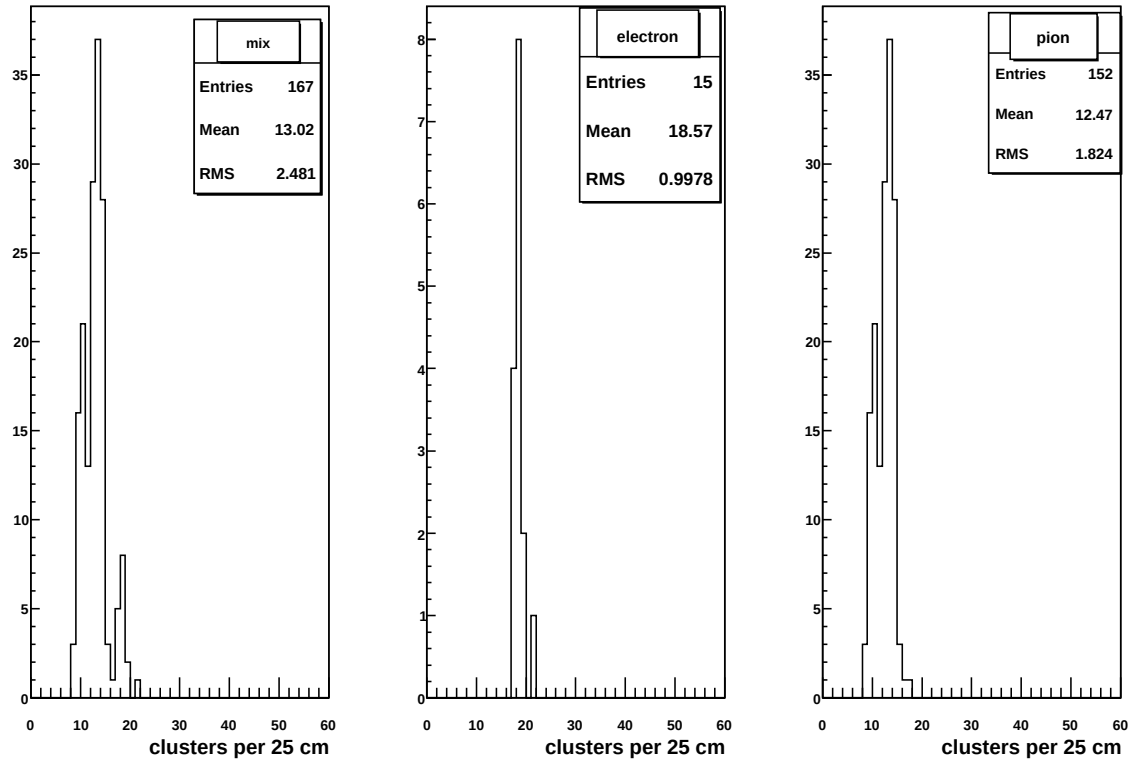

Figure 4.9: The number of clusters per cm in xenon 30% CO_2, calculated for each track (a) and for combined to 25 cm of track (b).

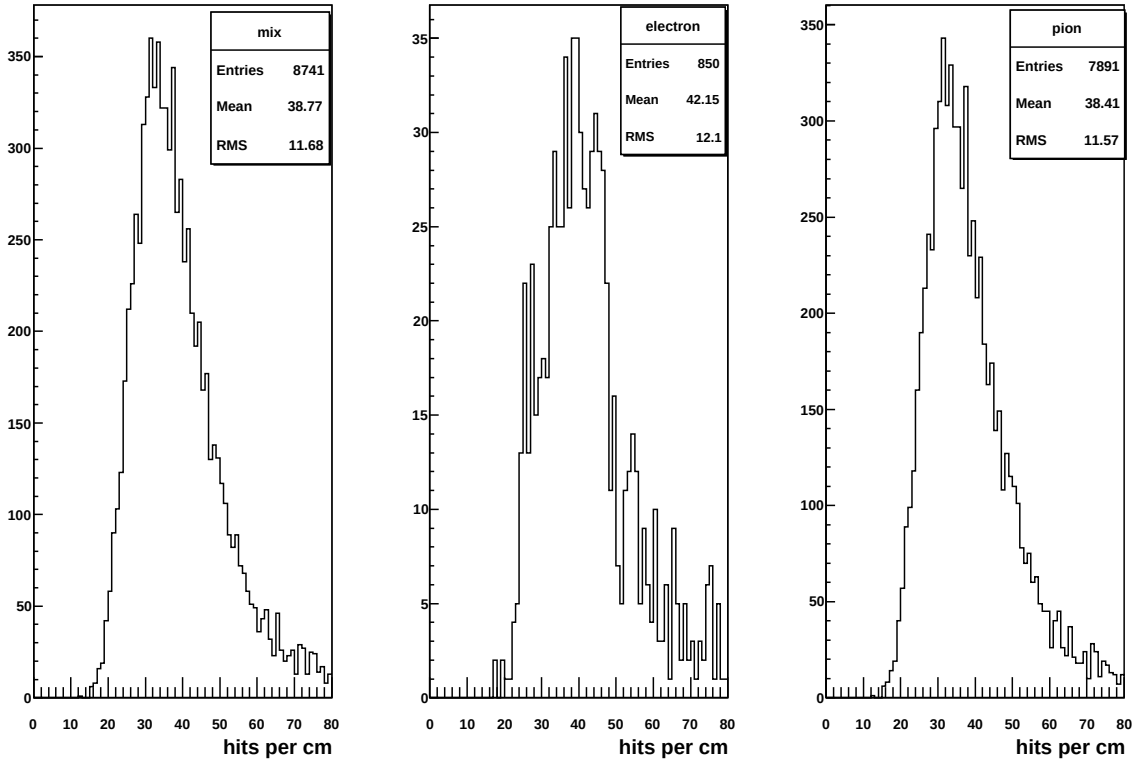

(a)

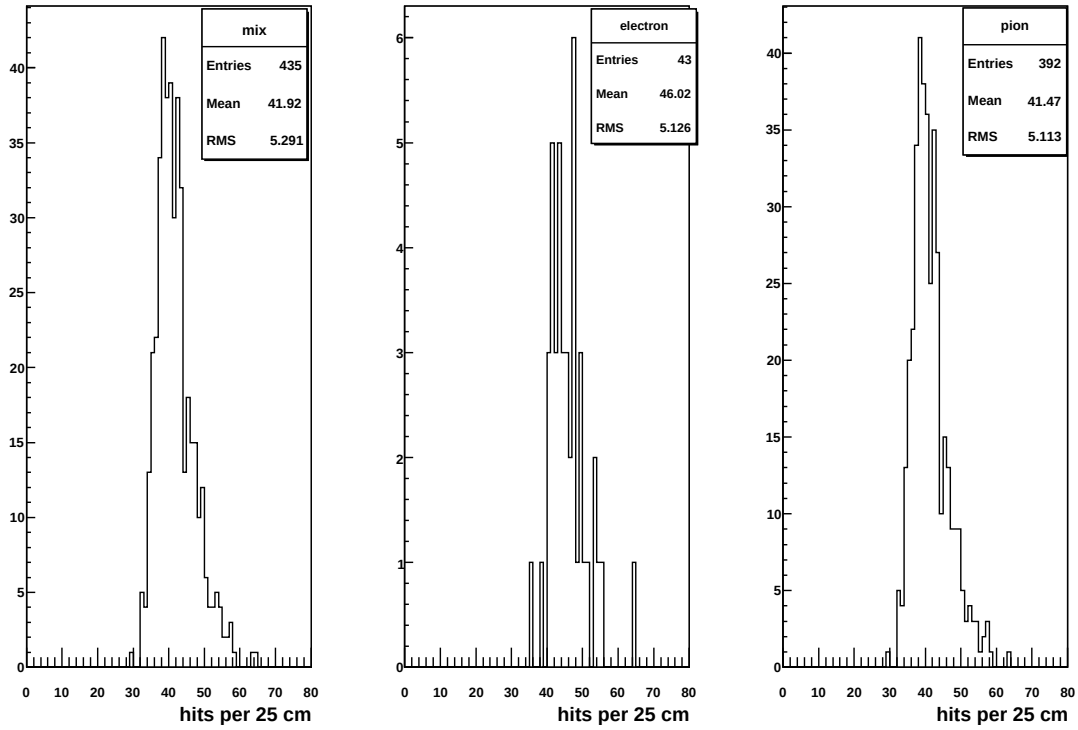

Figure 4.10: The number of hits per cm in helium 20% isobutane, calculated for each track (a) and for combined 25 cm of track (b).

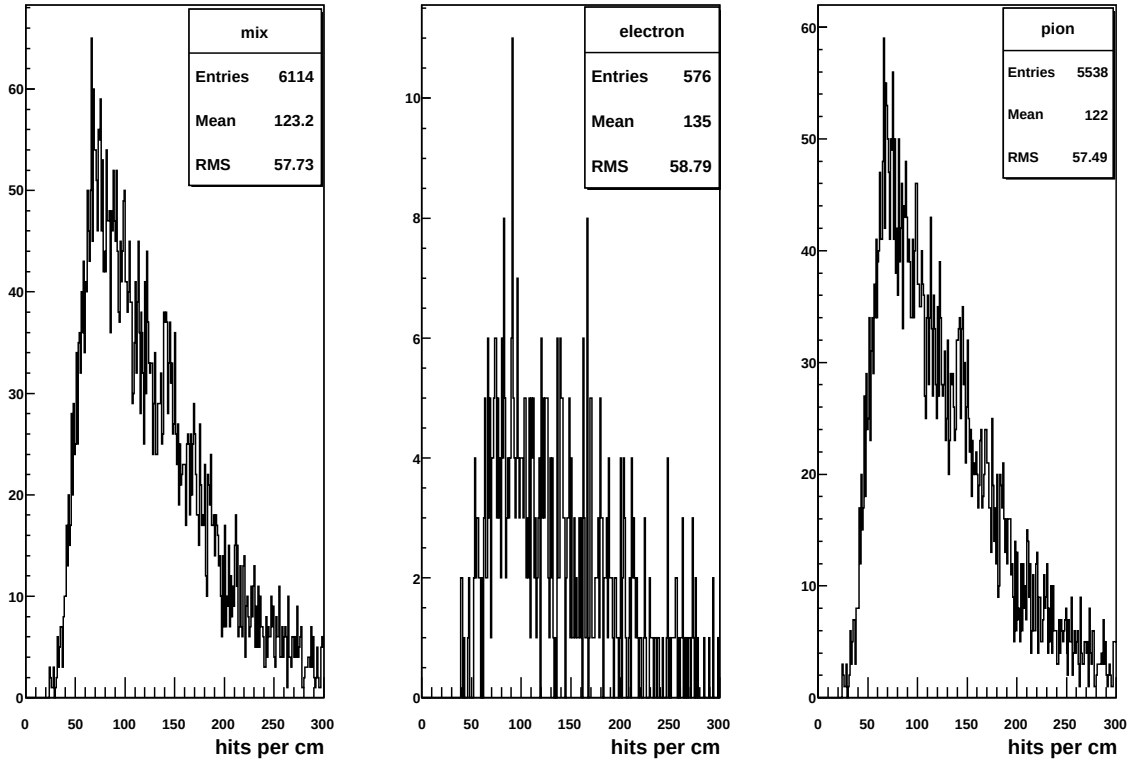

(a)

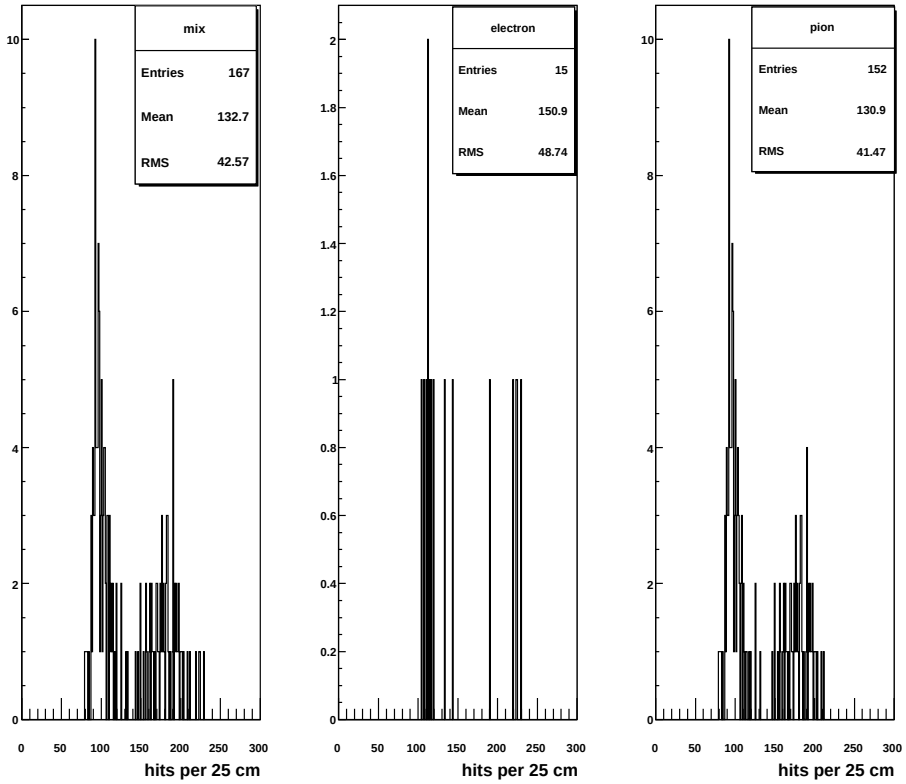

Figure 4.11: The number of hits per cm in xenon 30% CO_2, calculated for each track (a) and for combined 25 cm of track (b).

Chapter 5

Conclusions

From this research, it can be concluded:

- From section 3.1 that the GridPix detector can successfully be operated in a magnetic field up to 1T.
- From section 3.4 that a Hough Transformation can in general be used to recognise (multiple) tracks in GridPix data.
- From section 4.2 that the residuals in the z-direction are not measured correctly, likely due to time slewing effects, hampering a zero point resolution measurement in this direction.
- From section 4.2 that it is useful to remove multi pixel hits from the raw data files before further analysis in order to improve fitting results.
- From section 4.3.1 that the method chosen in this research allows to derive the transverse diffusion.
- From section 4.3.2 that the inclusion of a magnetic field decreases transverse diffusion significantly for argon 3% CF_4 2% isobutane, but not as much as expected from MAGBOLTZ calculations.
- From section 4.3.1 and 4.3.2 that the reconstructed transverse diffusion coefficient depends on the value of z_{max}, which is not exactly constant, is affected by time slewing effects and the delay between concidence and trigger, imposing a large error on the measured values.
- From section 4.4 that the usage of a decreasing exponential function for the determination of the energy loss results in values compatible with expectations from MAGBOLTZ, with 1 cm track length.
- From section 4.4 that in helium 20% isobutane 5 GeV pions can be distinguished from 5 GeV electrons with 4.4σ confidence level for 25 cm of track length.
- From section 4.4 that in xenon 30% CO_2 5 GeV pions can be distinguished from 5 GeV electrons with 2.9σ confidence level for 25 cm of track length.
- The measured values for drift velocity and transverse diffusion in this research are not always compatible with calculations from MAGBOLTZ.

Chapter 6

Outlook

At the moment of writing no collisions can be expected in the LHC's experiments for the next months. This does not mean R&D for possible upgrades of the experiments or other new detectors should be slowed down. It is important to do research, even if its outcome or use is not always clear at the moment when the research is done.

Working in an R&D group provided me with a different view on working in a scientific environment, a very practical one, which I liked. I learned that without detectors there can be no measurement, and without R&D no progress.

To optimise the research on the GridPix characteristics, it is advisable that the drift velocity is measured as accurately as possible for every gas mixture used. For many gas mixtures tedious drift velocity measurements have been done. But circumstances may differ for each measurement and in order to compare results it is important to know the drift velocity for each run. In this specific case, it would have been better if for each gas mixture used a run would have been taken under a 25° angle during the beam test at CERN. If the GridPix is used in a larger experiment there are other possibilities to measure the drift velocity externally in the gas unambiguously.

In order to improve the results of the zero point resolution measurements, three provisions could be taken. Firstly, the moment of gate opening, which determines the z_{max} for that particular measurement, needs to be assessed. This could be done by sending the delayed trigger signal to one pixel on the chip externally. In this way, possible timing jitter in the gate opening can be monitored and corrected for. Secondly, the delay between coincidence and gate opening needs to be measured precisely. If this delay is not known, electrons that have drifted some distance during the delay are measured to have zero drift and alter the measured drift distance for a part of the track. Thirdly, it would be very useful to correct for time slewing for each pixel, by also measuring pulse height simultaneously with the timing information. This could also be useful if one wants to give a weight to pixels or clusters in the fit. At the moment of writing, work is in progress on the TimePix2 chip, on which each pixel will conduct both a Time and a pulse height measurement. Moreover it would be interesting to use another way to reconstruct the zero point resolution, as from this thesis it is not concluded that the resolution can be found by extrapolating the fit of the variances of the residuals.

For an estimate of the zero point resolution in the z-direction, it is necessary to improve the fitting results in that direction. This could be done by removing all multi pixel hits and under-

standing and removing the influences from time slewing effects. Probably more investigation will be needed on this matter.

It is very promising that the distinction between electrons and pions proved itself possible with these detectors and this analysis. In this thesis we found that 25 cm of track length allows particle identification with a confidence level of 4.4σ in helium 20% isobutane. With track lengths of 1.2 m, like in the ILC detector would be the case, an electron will create around 3000 ionisations along its total track length. The relative error on the number of ionisations will become of the order of 2-3%, enabling trustable particle identification using one track.

The GridPix can still be an interesting candidate for tracking at the ILC. At the moment of writing, there is work in progress to increase the active surface from 14x14mm to 112x112mm. With gas as an active medium, the GridPix potentially needs little power. With a larger active surface, low power consumption and a light active medium, the detector can mean a lot to future experiments.

Chapter 7

Samenvatting

Het is met enige melancholie dat ik nu achter de computer zit om het afgelopen jaar samen te vatten voor het laatste hoofdstuk van deze scriptie. Als afsluiting van de master Particle and Astro Particle Physics van de Universiteit van Amsterdam, heb ik een jaar een research project gedaan bij de R&D afdeling van het Nikhef in Amsterdam. Vlak voordat ik bij de R&D groep aan de slag ging, was er een doorbraak geweest bij de ontwikkeling van een nieuw soort detector, genaamd GridPix. Aan mij de opdracht om metingen met deze detector te doen in een magneetveld, mee te gaan naar een beam test op CERN en al deze metingen te analyseren.

Het principe van de GridPix is dat van de time projection chamber, of TPC. Een TPC is een gas volume met een uitlezing aan een of beide kanten. Geladen deeltjes die door het gas vliegen, maken elektronen en ionen vrij langs hun baan. Onder de invloed van een elektrisch veld in de detector, driften de elektronen naar een anode. Op de anode worden ze uitgelezen, veelal na versterking van het signaal. In het geval van de GridPix is de anode een chip die gevoelig is voor lading. Zoals de chip in een digitale camera gevoelig is voor licht. Boven de chip is een dun folie met gaatjes, het Grid, aangebracht. Tussen het Grid en de chip staat een hoog elektrisch veld, waarin de driftende elektronen versneld worden en zo een lawine van elektronen maken op de chip. Op de chip zelf is een laag aangebracht om de chip te beschermen tegen gasontladingen in het gas.

Als de elektronen zijn losgemaakt in het gas, botsen ze onderweg tegen gas moleculen en driften dus niet in een rechte lijn naar de chip. Dat proces heet diffusie. Door diffusie kan de gemeten plaats van het elektron afwijken van de projectie plaats van creatie. Het is dus zaak de diffusie zo klein mogelijk te maken. Ook als elektronen niet driften heeft de detector een eindige resolutie, de zogenaamde *zero point resolutie*. Voor mijn afstudeerproject heb ik de diffusie coefficiënten in verschillende gas mengels gemeten en de zero point resolutie geprobeerd te bepalen.

De hoeveelheid ionisaties in het gas hangt af van luchtdruk, temperatuur, het gas mengsel en de impuls en identiteit van het passerende deeltje. Als de eerste vier gelijk blijven, is het dus mogelijk om de identiteit van het deeltje te achterhalen door het aantal ionisaties in het gas te reconstrueren. Ook dat was een onderdeel van mijn project.

De metingen die ik heb gedaan in Amsterdam dienden vooral om te bepalen of de diffusie meetbaar kleiner wordt onder invloed van een magneetveld. Dat bleek het geval, maar het effect lijkt kleiner dan te verwachten mag worden naar aanleiding van berekeningen. Ook is meteen aangetoond dat de detector gebruikt kan worden in een magneetveld.

Gebruikmakend van de vele metingen die wij op CERN hadden gedaan, heb ik de diffusie bepaald in verschillende gas mengsels. Voor het gas mengsel helium 20% isobutaan komt de gemeten waarde overeen met de verwachte waarde. Voor de andere onderzochte gassen zijn er verschillen tussen de gemeten waarde en de verwachte waarde. Deze verschillen zijn toe te schrijven aan verschillen in gemeten en verwachte drift snelheid van de elektronen, een niet precies bekende vertraging tussen passage van het deeltje en de start van de uitlezing van de detector en het feit dat de detector niet altijd precies even lang wordt uitgelezen.

De zero point resolutie is in dit onderzoek slechts met grote fout bepaald. Dat komt door dezelfde problemen als beschreven in de vorige paragraaf en door het feit dat een pixel niet meteen gaat meten als een signaal binnen komt. Dat effect heet time slewing en verstoort een goede tijdsbepaling van de metingen.

De bepaling van het energieverlies van de deeltjes, of te wel het aantal ionisaties per lengte eenheid spoor, resulteerde in de opvallende observatie dat elektronen van pionen kunnen worden onderscheiden met een zekerheid van 4.4σ als de tracks achter elkaar worden geplakt tot een totale lengte van 25 cm. In een mogelijke toekomstige toepassing van deze detector, zal de track lengte in de orde van 1.2 m zijn en zal de onderscheiding dus nog preciezer zijn.

Naar aanleiding van mijn onderzoek mag geconcludeerd worden dat de R&D voor de GridPix detectors nog niet voltooid is, maar dat de detector zeker een kandidaat kan zijn om gebruikt te worden in toekomstige grote deeltjes fysica experimenten. Verder heb ik in het afgelopen jaar veel geleerd en heeft onder andere dit project mij doen besluiten in de natuurkunde door te willen gaan.

Chapter 8

Appendix A

gas	E_{drift} (V/cm)	$-V_{grid}$ (V)	PID	p (GeV)	N_{trig}	run
Ar 3% CF_4 2% IsoB	200	320	none	5	1015	01010201
Ar 3% CF_4 2% IsoB	200	340	none	5	1014	01010202
Ar 3% CF_4 2% IsoB	200	360	none	5	1015	01010203
Ar 3% CF_4 2% IsoB	200	360	none	2	1716	01010101
Ar 3% CF_4 2% IsoB	200	360	elec	2	1027	01010204
Ar 3% CF_4 2% IsoB	200	360	pi	2	1371	01010205
Ar 3% CF_4 2% IsoB	200	320	none	5	1015	01010206
Ar 3% CF_4 2% IsoB	200	320	none	5	1028	01010102
Ar 3% CF_4 2% IsoB	200	340	none	5	1014	01010207
Ar 3% CF_4 2% IsoB	200	360	none	5	1015	01010208
Ar 30% CO_2	470	430	none	5	1038	01020201
Ar 30% CO_2	470	440	none	5	1157	01020202
Ar 30% CO_2	470	440	none	5	987	01020302
Ar 30% CO_2	470	460	none	5	1050	01020203
Ar 30% CO_2	470	460	none	5	1019	01020204
Ar 30% CO_2	470	460	none	5	1012	01020304
Xe 30% CO_2	1000	490	elec	5	445	01040101
He 20% IsoB	560	400	elec + pi	5	2378	02030101
He 20% IsoB	560	420	elec + pi	5	3575	02030102
He 20% IsoB	560	440	elec + pi	5	1053	02030103
He 20% IsoB	560	440	elec + pi	5	1568	02030104
He 20% IsoB	560	440	elec + pi	5	1080	02030105
He 20% IsoB	560	440	elec + pi	5	1257	02030106
He 20% IsoB	560	440	elec + pi	5	617	02030107
He 20% IsoB	560	440	elec + pi	5	336	02030108
He 20% IsoB	560	440	elec + pi	5	1131	02030109
He 20% IsoB	560	440	elec + pi	5	1090	02030110
He 20% IsoB	560	440	elec + pi	5	877	02030111
He 20% IsoB	560	440	elec + pi	5	228	02030112
He 20% IsoB	560	440	elec + pi	5	1234	02030113
He 20% IsoB	560	440	elec + pi	5	1333	02030114
He 20% IsoB	560	440	elec + pi	5	1068	02030115
He 20% IsoB	560	440	elec + pi	5	1048	02030116
He 20% IsoB	560	440	elec + pi	5	1008	02030117
Xe 30% CO_2	1400	440	elec	5	1045	02040111
Xe 30% CO_2	1400	440	elec	5	1124	02040112
Xe 30% CO_2	1400	440	elec	5	6708	02040113
Xe 30% CO_2	1900	460	elec	5	308	02040114
Xe 30% CO_2	1900	460	elec	5	414	02040115
Xe 30% CO_2	1900	465	elec	5	535	02040116
Xe 30% CO_2	1900	465	elec	5	1305	02040117
Xe 30% CO_2	1900	470	elec	5	1133	02040118

Table 8.1: Measurements performed at CERN. N_{trig} stands for the number of triggers during a run. The coding for the runs represents the chip used, the gas mixture, the placement of the scintillator and the number of the run.

gas	E_{drift} (V/cm)	D_t exp ($\mu m/\sqrt{cm}$)	D_t measured ($\mu m/\sqrt{cm}$)	$\sigma_{xy,0}$ (μm)
Ar 3% CF_4 2% IsoBut	200	290	168 ± 8	-20±14
Ar 3% CF_4 2% IsoBut	200	290	118 ± 6	36±10
Ar 3% CF_4 2% IsoBut	200	290	104 ± 5	44±9
Ar 3% CF_4 2% IsoBut	200	290	152 ± 7	14±13
Ar 3% CF_4 2% IsoBut	200	290	138 ± 7	16±12
Ar 3% CF_4 2% IsoBut	200	290	156 ± 8	15±13
Ar 3% CF_4 2% IsoBut	200	290	106 ± 13	85±9
Ar 3% CF_4 2% IsoBut	200	290	130 ± 6	43±10
Ar 3% CF_4 2% IsoBut	200	290	137 ± 7	84±11
Ar 30% CO_2	470	148	89 ± 4	22±7
Ar 30% CO_2	470	148	84 ± 4	25±7
Ar 30% CO_2	470	148	31 ± 2	24±3
Ar 30% CO_2	470	148	72 ± 4	22±6
Ar 30% CO_2	470	148	74 ± 4	29±6
Ar 30% CO_2	470	148	29 ± 4	22±3
Xe 30% CO_2	1000	185	40 ± 8	30±15
He 20% IsoBut	560	175	188 ± 9	21±15
He 20% IsoBut	560	175	186 ± 9	20±15
He 20% IsoBut	560	175	186 ± 9	23±15
He 20% IsoBut	560	175	185 ± 9	14±15
He 20% IsoBut	560	175	178 ± 9	25±14
He 20% IsoBut	560	175	181 ± 9	23±15
He 20% IsoBut	560	175	168 ± 8	24± 13
He 20% IsoBut	560	175	174 ± 9	27±15
He 20% IsoBut	560	175	169 ± 8	28± 14
He 20% IsoBut	560	175	123 ± 17	23± 10
He 20% IsoBut	560	175	187 ± 9	25± 15
He 20% IsoBut	560	175	179 ± 9	24± 15
He 20% IsoBut	560	175	197 ± 9	24± 16
He 20% IsoBut	560	175	169 ± 10	27± 13
He 20% IsoBut	560	175	173 ± 8	25±14
He 20% IsoBut	560	175	171 ± 9	31±14
He 20% IsoBut	560	175	176 ± 8	23±15
Xe 30% CO_2	1400	103	134 ± 7	30±11
Xe 30% CO_2	1400	103	134 ± 8	20± 11
Xe 30% CO_2	1400	103	134 ± 7	20± 11
Xe 30% CO_2	1900	110	171 ± 8	18±14
Xe 30% CO_2	1900	110	163 ± 10	16± 14
Xe 30% CO_2	1900	110	174 ± 8	21± 14
Xe 30% CO_2	1900	110	171 ± 8	12± 14
Xe 30% CO_2	1900	110	176 ± 9	19± 14

Table 8.2: Expected and measured transverse diffusion coefficients and zero point resolution in the x/y-plane, $\sigma_{xy,0}$, for all test beam runs. The results in each block between horizontal lines in this table are used to calculate the combined values listed in table 4.2. The grid voltages for these measurements can be found in table 8.1.

gas	particle	n_p/cm expected	n_p/cm measured
Ar 3% CF_4 2% IsoBut	elec	22.2	22.6 ± 1.6
	pi	18.2	18.6 ± 1.4
Xe 30% CO_2	elec	16.7	11.0 ± 0.5
	pi	14.7	7.9 ± 0.9
Xe 30% CO_2	elec	16.7	11.7 ± 0.4
	pi	14.7	7.5 ± 1.0
Xe 30% CO_2	elec	16.7	10.7 ± 0.3
	pi	14.7	7.6 ± 0.7
Xe 30% CO_2	elec	16.7	11.4 ± 0.8
	pi	14.7	7.6 ± 0.4
Xe 30% CO_2	elec	16.7	11.8 ± 0.8
	pi	14.7	7.6 ± 0.4
Xe 30% CO_2	elec	16.7	11.5 ± 0.6
	pi	14.7	7.9 ± 0.3
Xe 30% CO_2	elec	16.7	11.6 ± 0.7
	pi	14.7	7.8 ± 0.9
Xe 30% CO_2	elec	16.7	11.2 ± 0.8
	pi	14.7	7.9 ± 0.2
He 20% IsoBut	elec	24.9	27.7 ± 0.4
	pi	21.9	23.5 ± 0.1
He 20% IsoBut	elec	24.9	27.6 ± 0.5
	pi	21.9	22.1 ± 0.2
He 20% IsoBut	elec	24.9	23.9 ± 0.5
	pi	21.9	21.3 ± 0.1
He 20% IsoBut	elec	24.9	24.8 ± 0.5
	pi	21.9	22.0 ± 0.2
He 20% IsoBut	elec	24.9	24.7 ± 0.5
	pi	21.9	21.1 ± 0.2
He 20% IsoBut	elec	24.9	26.5 ± 1.1
	pi	21.9	21.7 ± 0.3
He 20% IsoBut	elec	24.9	25.6 ± 0.7
	pi	21.9	20.8 ± 0.2
He 20% IsoBut	elec	24.9	27.9 ± 0.7
	pi	21.9	20.0 ± 0.2
He 20% IsoBut	elec	24.9	25.5 ± 0.7
	pi	21.9	19.4 ± 0.2
He 20% IsoBut	elec	24.9	25.8 ± 1.7
	pi	21.9	18.6 ± 0.4
He 20% IsoBut	elec	24.9	26.7 ± 0.6
	pi	21.9	19.1 ± 0.1
He 20% IsoBut	elec	24.9	26.4 ± 0.7
	pi	21.9	19.3 ± 0.2
He 20% IsoBut	elec	24.9	29.2 ± 0.7
	pi	21.9	20.2 ± 0.2
He 20% IsoBut	elec	24.9	26.9 ± 0.7
	pi	21.9	23.7 ± 0.2

Table 8.3: Expected and measured number of clusters per cm track for all test beam runs. Only runs performed with particle identification are used.

Bibliography

[1] http://public.web.cern.ch/public/en/LHC/LHC-en.html.

[2] James Brau, Yasuhiro Okada, Nicholas Walker (eds.), *international linear collider reference design report*, Executive Summary **1** (2007) .

[3] http://www.linearcollider.org/gateway/.

[4] http://www.linearcollider.org/pdf/ILCposterNEW-200702.pdf.

[5] James Brau, Yasuhiro Okada, Nicholas Walker (eds.), *international linear collider reference design report*, Detectors **4** (2007) .

[6] http://www.linearcollider.org/cms/?pid=1000472.

[7] S. Amsler *et al.*, *Review of particle physics*, Physics Letters B667 **1** (2008) .

[8] T. Behnke *et al.*, *Proposal for an ilc tpc data stream (draft)*, 2006.

[9] http//ilcsoft.desy.de.

[10] http://ilcsoft.desy.de/marlin.

[11] http//ilcsoft.desy.de/gear.

[12] http//lcio.desy.de/lccd.

[13] Konrad Kleinknecht, *detectors for particle radiation*, volume 2, Cambridge University Press, 1998.

[14] W. Blum and L. Rolandi, *Particle Detection with Drift Chambers*, volume 2, Springer Verlag, 1994.

[15] D. Nygren and J. Marx, *The time projection chamber*, Physics Today **31** (1978) 46.

[16] http://cerncourier.com/cws/article/cern/29014.

[17] A. Oed, *Position-sensitive detector with microstrip anode for electron multiplication with gases*, Nuclear Instruments and Methods A. **263** (1988) 351.

[18] F. Sauli, *Gem: A new concept for electron amplification in gas detectors*, Nuclear Instruments and Methods A. **386** (1977) 531.

[19] I. Giomataris *et al.*, *Micromegas: a high-granularity position-sensitive gaseous detector for high particle-flux environments*, Nuclear Instruments and Methods A. **376** (1996) 29.

[20] http://www.nikhef.nl/pub/experiments/medipix/muros.html.

[21] http://aladdin.utef.cvut.cz/ofat/others/Pixelman/index.html.

[22] http://147.32.68.57/ofat/Methods/TimePixCalibration/index.htm.

[23] X. Llopart *et al.*, *Timepix, a 65k programmable pixel readout chip for arrival time, energy and/or photon counting measurements*, Nuclear Instruments and Methods A. **581** (2007) 485.

[24] Stephen Biagi, http://consult.cern.ch/writeup/magboltz/.

[25] http://planetmath.org/encyclopedia/HoughTransform.html.

[26] E. de Wolf, *Statistical Data Analysis, course notes for University of Amsterdam*, 2007.

[27] William, A. P. and others, *Numerical recipes in C++*, volume 2, Cambridge University Press, 2002.

[28] http://root.cern.ch/root/htmldoc/MATH-MINUIT2-Index.html.

[29] http:cern.root.ch.